2.13.7

Molecular dynamics methods in microscale heat transfer

Shigeo Maruyama

A. Introduction

In normal heat transfer and fluid flow calculations, the fluid phases are treated as being *continuous* with properties such as viscosity and thermal conductivity being assumed to be only a function of local pressure, composition and temperature in the flow domain. However, as the size of the flow domain (the channel) becomes smaller and smaller, the continuum treatment breaks down since, in reality, the fluid consists of molecules and, when the flow domain size is no longer enormously greater than molecular scale, the fluid must be considered in terms of collections of molecules. This situation is approached in microscale heat transfer and fluid flow.

Molecular level understandings are becoming more important and molecular based simulations are becoming more practical for microscale and nanoscale heat transfer problems. For example, studies of basic mechanisms of heat transfer such as in phase change heat transfer demand the microscopic understanding of liquid-solid contact phenomena. Efficient heat transfer at three-phase interfaces (evaporation and condensation of liquid on a solid surface) becomes the singular problem in the macroscopic treatment. The nucleation theory of liquid droplet in vapor or of vapor bubble in liquid sometimes needs to take account of nuclei in the size range of molecular clusters. The effect of the surfactant on the heat and mass transfer through liquid-vapor interface is also an example of the direct effect of molecular scale phenomena on the macroscopic problem. Even though there has been much effort of extending our macroscopic analysis to extremely microscopic conditions in space (micrometer scale and nanometer scale system), time (microsecond, nano-second and picosecond technology), and rate (extremely high heat flux), there are certain limitations in the extrapolations. Hence, the bottom-up approach from the molecular level is very important.

On the other hand, recent advances in microscale and nanoscale heat transfer and in nanotechnology require the detailed understandings of phase change and heat and mass transfer in nanometer and micrometer scale regimes. The mechanical and chemical engineering processes to create nanoscale structures such as carbon nanotubes, or fluid phase change confined in nanoporous material are examples. The wetting of liquid or absorption is more important since the adhesive force is extremely important for small systems and creation of extremely large surface area is possible with nanoscale structures. The use of molecular dynamics simulations is straightforward for such nanoscale systems. Here, again, it is practically important to compare such nanoscale phenomena with macroscopic phenomena, because an analogy to the larger system is often an important strategy in order to understand a nanoscale phenomenon. An important feature intrinsic to a nanoscale system is usually found through the rational comparison with a macroscopic system. Furthermore, it should be noted that so-called microscale heat transfer often deals with simply macroscopic problems from the nanoscale and molecular scale point of view.

In this Section, one of the promising numerical techniques, the classical molecular dynamics method, is overviewed with a special emphasis on applications to inter-phase and heat transfer problems. Molecular dynamics methods have long been used and are well developed as a tool in statistical mechanics and chemistry [1, 2]. However, it is a new challenge to extend the method to the spatial and temporal scales of macroscopic heat transfer phenomena [3-5]. On the

other hand, the thin film technology related to the semiconductor industry and recent nanotechnology demand the prediction of heat transfer characteristics of nanometer scale materials [6].

In addition to a brief description of the basic concept of molecular dynamics method, various examples of potential functions as Lennard-Jones potential for rare gas, effective pair potential for water, alcohols and organic molecules, many-body potential for silicon and carbon, and embedded atom potential for solid metals are discussed. Depending on the nature of electronic structure or simply bonding characteristics, suitable choice of potential functions is extremely important for realistic simulations. Several examples of potential functions between heterogeneous systems are found in later part such as between water-solid platinum, hydrogen-graphite (carbon nanotube), water-graphite (carbon nanotube) and metal-carbon. Various techniques to obtain thermodynamic and thermo-physical properties from the equilibrium or non-equilibrium simulations are explained.

Examples of various applications of molecular dynamics simulations follow in Section 2.13.7C. After the brief discussion of the liquid-vapor interface characteristics such as the surface tension, the Young-Laplace equation and condensation coefficient, solid-liquid-vapor interaction characteristics such as liquid contact phenomena and absorption phenomena are discussed from a molecular standpoint. In addition to the simple Lennard-Jones system discussed in a previous review [3], a simulation of water liquid droplet in contact with platinum solid surface is introduced. Because a water molecule makes a hydrogen bond, the contact phenomena are drastically different from the simple Lennard-Jones fluid. The water droplet exhibits a finite contact angle on the absorbed monolayer water film. The contact angle is determined by the surface energy between this monolayer water film and the bulk liquid water film. In addition to the macroscopic problems, several nanoscale contact and absorption problems related to carbon nanotubes are also discussed.

Topics in nucleation and phase change phenomena include homogeneous nucleation of a liquid droplet for a Lennard-Jones fluid and water, and heterogeneous nucleation of liquid droplet and vapor bubble on a solid surface for simple Lennard-Jones fluid. In addition, an example of crystallization process of amorphous silicon is discussed. The nucleation process of molecules such as fullerene and single walled carbon nanotubes are also discussed as the connection to nanotechnology.

Among 3 modes of heat transfer, heat conduction, convective heat transfer and radiative heat transfer, only heat conduction can be directly accessed by the current scale of molecular dynamics simulations. Several topics of heat conduction such as the thermal boundary resistance between solid materials and solid-liquid interfaces, and heat conduction along a carbon nanotube

are discussed.

B. Molecular dynamics method

Knowledge of statistical mechanical gas dynamics has been helpful to understand the relationship between molecular motion and macroscopic gas dynamics phenomena [7]. Recently, a direct simulation method using the Monte Carlo technique (DSMC) developed by Bird [8] has been widely used for the practical simulations of rarefied gas dynamics. On the other hand, statistical mechanical treatment of solid-state matters has been well developed in solid state physics [e.g. 9]. For example, the direct simulation of the Boltzmann equation of phonon dynamics is being developed and applied to the heat conduction analysis of thin films [10]. However, when we need to consider a liquid or inter-phase phenomenon, which is inevitable for phase-change heat transfer, the statistical mechanics approach is not as well developed as for the gas-dynamics statistics and the solid-state statistics. The most powerful tool for the investigation of the microscopic phenomena in heat transfer is the molecular dynamics method [e.g. 1-3]. In principal, the molecular dynamics method can be applied to all phases of gas, liquid and solid and to interfaces of these three phases.

(a) Equation of motion and potential Function

In the classical molecular dynamics method, the equations of motion (Newton's equations) are solved for atoms as

$$m_i \frac{d^2 \mathbf{r}_i}{dt^2} = \mathbf{F}_i = -\Delta_i \Phi \,, \qquad (1)$$

where m_i, r_i, F_i are mass, position vector, force vector of molecule i, respectively, and Φ is the potential of the system. This classical form of equation of motion is known to be a good approximation of the Schrödinger equation when the mass of atom is not too small and the system temperature is high enough compared with the gap of quantum energy levels associated with the dynamics. For translational and rotational motions of molecules, Equation (1) can be valid except for light molecules such as hydrogen and helium and except at cryogenetic temperature. On the other hand, some quantum corrections are sometimes critical for intra-molecule vibrational motion of small molecules even at room temperature. Once the potential of a system is obtained, it is straightforward to numerically solve Eq. (1). In principal, any of the gas, liquid, solid states, and inter-phase phenomena can be solved without the knowledge of "thermo-physical properties" such as thermal conductivity, viscosity, latent heat, saturation temperature and surface tension.

The potential of a system $\Phi(\mathbf{r}_1, \mathbf{r}_2, ... \mathbf{r}_N)$ can often be reasonably assumed to be the sum of the effective pair potential $\phi(r_{ij})$ as

$$\Phi = \sum_i \sum_{j>i} \phi(r_{ij}), \qquad (2)$$

where r_{ij} is the distance between molecules i and j. It should be noted that the assumption of Eq. (2) is often employed for simplicity even though the validity is questionable. In the following examples, the potential functions for covalent system such as carbon and silicon and embedded atom models for solid metal do not use this approximation.

(b) Examples of potential functions

In order to simulate practical molecules, the determination of the suitable potential function is very important. Here, the well-known Lennard-Jones potential for van der Waals interactions, potential forms for water and larger molecules, multi-body potential for silicon and carbon, and embedded atom model for solid metals are reviewed.

I. Lennard-Jones potential

The most widely used pair potential for molecular dynamics simulations is Lennard-Jones (12-6) potential function expressed as

$$\phi(r) = 4\varepsilon \left[\left(\frac{\sigma}{r} \right)^{12} - \left(\frac{\sigma}{r} \right)^6 \right], \qquad (3)$$

where ε and σ are energy and length scales, respectively, and r is the intermolecular distance as shown in Fig. 1. The intermolecular potential of inert monatomic molecules such as Ne, Ar, Kr and Xe is known to be reasonably expressed by this function with the parameters listed in Table 1. Moreover, many computational and statistical mechanical studies have been performed with this potential as the model pair potential. Here, the equation of motion can be non-dimensionalized by choosing σ, ε and m as length, energy and mass scale, respectively. The reduced formulas for typical physical properties are listed in Table 2. When a simulation system consists of only Lennard-Jones molecules, the non-dimensional analysis
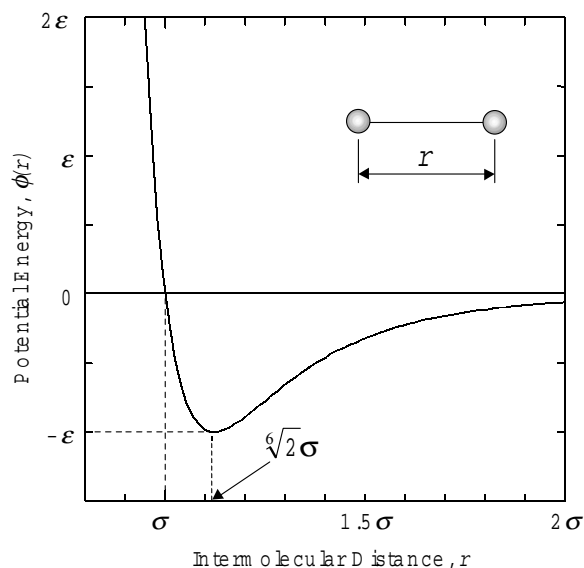

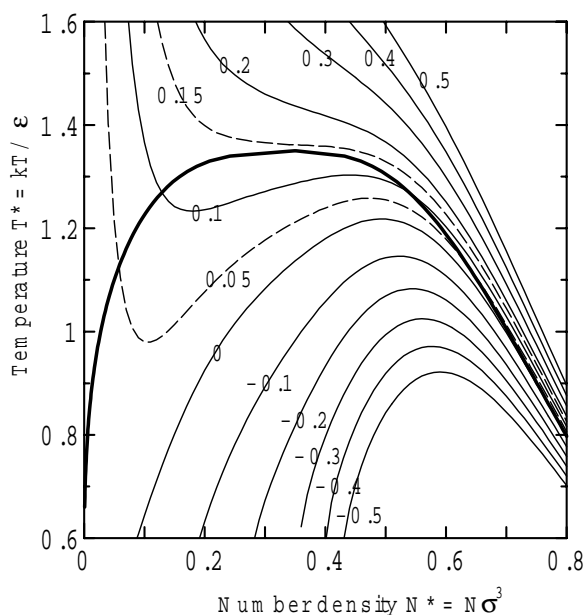**Figure 1** Lennard-Jones 912-6) potential.

Table 1 Parameters for Lennard-Jones potential for inert gas molecules

	σ [nm]	ε [J]	ε/k_B [K]
Ne	0.274	0.50×10^{-21}	36.2
Ar	0.340	1.67×10^{-21}	121
Kr	0.365	2.25×10^{-21}	163
Xe	0.398	3.20×10^{-21}	232

Table 2 Reduced properties for Lennard-Jones system.

Property		Reduced Form
Length	$r^* =$	r/σ
Time	$t^* =$	$t/\tau = t(\varepsilon/m\sigma^2)^{1/2}$
Temperature	$T^* =$	$k_B T/\varepsilon$
Force	$f^* =$	$f\sigma/\varepsilon$
Energy	$\phi^* =$	ϕ/ε
Pressure	$P^* =$	$P\sigma^3/\varepsilon$
Number density	$N^* =$	$N\sigma^3$
Density	$\rho^* =$	$\sigma^3\rho/m$
Surface tension	$\gamma^* =$	$\gamma\sigma^2/\varepsilon$

has the advantage in avoiding the need to repeat practically the same simulation. Then, molecules are called Lennard-Jones molecules, and argon parameters $\sigma = 0.34$ nm, $\varepsilon = 1.67 \times 10^{-21}$ J, and $\tau = 2.2 \times 10^{-12}$ s are often used to describe dimensional values in order to illustrate the physical meaning. The phase-diagram of Lennard-Jones system [11, 12] is useful for a design of a simulation. An example of the phase-diagram using the equations by Nicolas et al. [11] is shown in Fig. 2. Here, the critical and triplet temperatures are $T_c^* = 1.35$ and $T_t^* = 0.68$, or $T_c = 163$ K and $T_t = 82$ K for argon properties [13].

Figure 2 Phase diagram of Lennard-Jones fluid based on the state of equation by Nicolas et al.

For the practical calculation of potential, which is the most CPU demanding, Lennard-Jones function in Eq. (3) is cutoff at the intermolecular distance $r_C = 2.5\sigma$ to 5.5σ. In order to reduce the discontinuity at the cut-off point, several forms of smooth connection have been proposed such as by Stoddard & Ford [14]. However, for pressure or stress calculations, a contribution to the potential from far-away molecules can result in a considerable error as demonstrated for surface tension [15]. The smooth connection of the potential is not helpful at this critical point. At least for homogeneous system, the long-range correction technique described in Section 2.13.7B(f) can be used. For this purpose, the simple cut-off has an advantage. Here, the recommended strategy is to use the simple cut-off.

II. Effective pair potential for water

The effective pair potential form for water has been intensively studied. The classical ST2 potential proposed in 1974 by Stillinger and Rahman [16] based on BNS model [17] was widely used in the 1980s. Later, much simpler forms of SPC (Simple Point Charge) [18] and SPC/E (Extended SPC) [19] potentials were introduced by Berendsen et al. SPC/E potential employed the rigid water configuration in Fig. 3a, with the distance of OH just 0.1 nm and the angle of HOH the tetrahedral angle $\theta_t = 2\cos^{-1}\left(1/\sqrt{3}\right) \cong 109.47°$. The effective pair potential of molecules at R_1 and R_2 are expressed as the superposition of Lennard-Jones function of oxygen-oxygen interaction and the

Table 3 Potential parameters for water.

(a)

(b)
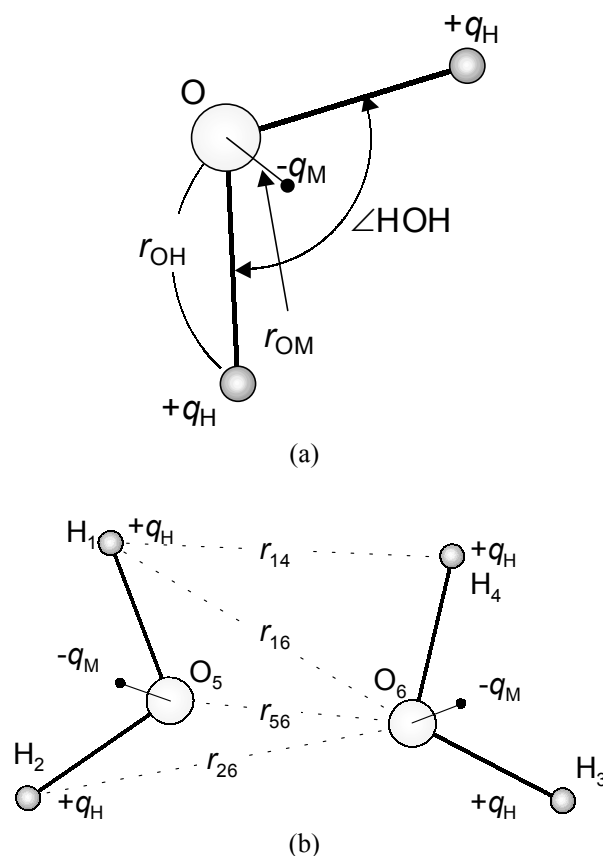
Figure 3 Classical rigid models of water for (a) 4 sites and 3 sites models, TIP4P, CC, SPC/E, (b) definition of interatomic length of CC potential.

electrostatic potential by charges on oxygen and hydrogen as follows.

$$\phi_{12}(\mathbf{R}_1, \mathbf{R}_2) = 4\varepsilon_{OO}\left[\left(\frac{\sigma_{OO}}{R_{12}}\right)^{12} - \left(\frac{\sigma_{OO}}{R_{12}}\right)^{6}\right]$$

$$+ \sum_i \sum_j \frac{q_i q_j e^2}{4\pi\varepsilon_0 r_{ij}}, \qquad (4)$$

where R_{12} represents the distance of oxygen atoms, and σ_{OO} and ε_{OO} are Lennard-Jones parameters. The Coulombic interaction is the sum of 16 pairs of point charges.

The TIP4P potential proposed by Jorgensen et al. [20] employed the structure of water molecule as $r_{OH} = 0.09572$ nm and $\angle HOH = 104.52°$ based on the experimentally assigned value for the isolated molecule. The positive point charges q were on hydrogen atoms, and the negative charge $-2q$ was set at r_{OM} from the oxygen atom on the bisector of the HOH angle, as in Fig. 3a. The parameters listed in Table 3 were optimized for thermodynamic data such as density,

		SPC/E	TIP4P	CC
r_{OH}	[nm]	0.100	0.095 72	0.095 72
$\angle HOH$	[°]	109.47	104.52	104.52
σ_{OO}	[nm]	0.316 6	0.315 4	N/A
$\varepsilon_{OO} \times 10^{-21}$	[J]	1.079 7	1.077 2	N/A
r_{OM}	[nm]	0	0.015	0.024 994
q_H [a]	[C]	0.423 8 e	0.52 e	0.185 59 e
q_M	[C]	-0.847 6 e	-1.04 e	-0.371 18 e

[a]Charge of electron e = 1.60219×10^{-19} C

potential energy, specific heat, evaporation energy, self-diffusion coefficient and thermal conductivity, and structure data such as the radial distribution function and neutron diffraction results at 25 °C and 1atm. This potential is regarded as one of the OPLS (optimized potential for liquid simulations) set covering liquid alcohols and other molecules with hydroxyl groups developed by Jorgensen [21].

MYC potential [22] and CC potential [23] were based on ab initio quantum molecular calculations of the water dimer with the elaborate treatment of electron correlation energy. The assumed structure and the distribution of charges are the same as TIP4P as shown in Fig. 3a with a different length r_{OM} and amount of charge as in Table 3. For CC potential, the interaction of molecules is parameterized as follows.

$$
\begin{aligned}
\phi_{12}(\mathbf{R}_1, \mathbf{R}_2) = & \sum_i \sum_j \frac{q_i q_j}{4\pi\varepsilon_0 r_{ij}} + a_1 \exp(-b_1 r_{56}) \\
& + a_2 \left[\exp(-b_2 r_{13}) + \exp(-b_2 r_{14}) \right. \\
& \left. + \exp(-b_2 r_{23}) + \exp(-b_2 r_{24}) \right] \\
& + a_3 \left[\exp(-b_3 r_{16}) + \exp(-b_3 r_{26}) \right. \\
& \left. + \exp(-b_3 r_{35}) + \exp(-b_3 r_{45}) \right] \\
& - a_4 \left[\exp(-b_4 r_{16}) + \exp(-b_4 r_{26}) \right. \\
& \left. + \exp(-b_4 r_{35}) + \exp(-b_4 r_{45}) \right]
\end{aligned}
\tag{5}
$$

$a_1 =$	315.708	$\times 10^{-17}$ [J],	$b_1 =$	47.555 [1/nm],
$a_2 =$	2.4873	$\times 10^{-17}$ [J],	$b_2 =$	38.446 [1/nm],
$a_3 =$	1.4694	$\times 10^{-17}$ [J],	$b_3 =$	31.763 [1/nm],
$a_4 =$	0.3181	$\times 10^{-17}$ [J],	$b_4 =$	24.806 [1/nm].

Among these rigid water models, SPC/E, TIP4P and CC potentials are well accepted in recent simulations of liquid water such as the demonstration of the excellent agreement of surface tension with experimental results using the SPC/E potential [24]. Because all of these rigid water models are "effective" pair potential optimized for liquid water, it must be always questioned if these are applicable to small clusters, wider range of thermodynamics conditions, or a liquid-vapor interface. Even though the experimental permanent dipole moment

of isolated water is 1.85 D[*], most rigid models employ higher values such as 2.351 D for SPC/E to effectively model the induced dipole moment at liquid phase. The direct inclusion of the polarizability to the water models results the many-body potential, which requires the iterative calculation of polarization depending on surrounding molecules. The polarizable potential based on TIP4P [25], MCY [26] and SPC [27] are used to simulate the structure of small clusters and transition of monomer to bulk properties. On the other hand, flexible water models with spring [28] or Morse type [29] intramolecular potential are used as a means of seeking for the demonstration of vibrational spectrum shift and for the reasonable prediction of dielectric constant.

III. Potential for larger molecules in the liquid phase (OPLS and AMBER)

For alcohol [21] and other larger hydrocarbon molecules with hydroxyl groups [30], the OPLS (optimized potential for liquid simulation) potential developed by Jorgensen is widely used. As mentioned in Section 2.13.7B(b)(II), TIP4P for water is one of the series of potentials. As in the case of water molecule, hydrogen atoms are not explicitly modeled but methyl and methylene units are treated as pseudo-atoms. All bond lengths are rigidly constrained to their equilibrium values. Methyl and methylene groups are labeled C_1 through C_n from the tail group, i.e., methyl group, to the head group, i.e., hydroxyl group. The interaction potential E_{AB} between two molecules A and B is determined by Coulomb and Lennard-Jones interactions between all intermolecular pairs of sites as follows.

$$
E_{AB} = \sum_i^A \sum_j^B \left[4\varepsilon_{ij} \left[\left(\frac{\sigma_{ij}}{r_{ij}} \right)^{12} - \left(\frac{\sigma_{ij}}{r_{ij}} \right)^6 \right] + \frac{q_i q_j e^2}{4\pi\varepsilon_0 r_{ij}} \right]
\tag{6}
$$

where q_i and q_j are the partial charges on united pseudo-atoms i and j, r_{ij} is the distance between these atoms. Because of all pairs of interaction of the Lennard-Jones term, Equation (6) is a little more complex than equation (4) for TIP4P water.

---

[*] 1 D = 3.3357×10^{-30} Cm in SI unit.

In order to obtain the Lennard-Jones potential parameters σ_{ij} and ε_{ij} for variety of combinations of molecules, the well known combination rule [31] as follows is used.

$$\sigma_{ij} = (\sigma_{ii} + \sigma_{jj}) / 2 \qquad (7)$$

$$\varepsilon_{ij} = \sqrt{\varepsilon_{ii} \varepsilon_{jj}} \qquad (8)$$

This combination rule is often used for obtaining Lennard-Jones parameter of unknown combinations.

The lowest energy intramolecular motion for a relatively long molecule is the internal rotation, or torsion. For a small molecule with a single dihedral angle, the following Fourier series can describe the potential energy for internal rotation.

$$E(\phi) = V_0 + \frac{1}{2}V_1(1 + \cos\phi) + \frac{1}{2}V_2(1 - \cos 2\phi)$$

$$+ \frac{1}{2}V_3(1 + \cos 3\phi) \qquad (9)$$

where ϕ is a dihedral angle and V_i are Fourier coefficients. For larger molecules, the number of freedom of internal rotations is increased but can be handled by using a Fourier series for each angle plus additional terms for non-bonded interactions between groups separated by more than three bonds.

The potential field for larger organic molecules and biological molecules such as protein and nucleic acid are much more complicated. The force field parameters obtained from molecular mechanics and accurate *ab initio* calculations are summarized as the AMBER force field by Kollman et al. [32-38]. Cornell et al. [34] used the following additive potential form.

$$E_{\text{pair}} = \sum_{\text{bonds}} K_r (r - r_{eq})^2 + \sum_{\text{angles}} K_\theta (\theta - \theta_{eq})^2$$

$$+ \sum_{\text{dihedrals}} \frac{1}{2}V_n \left[1 + \cos(n\phi - \gamma)\right]$$

$$+ \sum_{\text{van der Waals}}^{i<j} \left(\frac{A_{ij}}{R_{ij}^{12}} - \frac{B_{ij}}{R_{ij}^{6}} \right) + \sum_{\text{electro static}}^{i<j} \left(\frac{q_i q_j}{4\pi\varepsilon R_{ij}} \right)$$

$$\qquad (10)$$

with the bonds and angles represented by a simple diagonal harmonic expression, the van der Waals interaction represented by a Lennard-Jones potential, electrostatic interactions modeled by a Coulombic interaction of atom-centered point charges, and dihedral energies represented with a simple set of parameters.

Electrostatic and van der Waals interactions are only calculated between atoms in different molecules or for atoms in the same molecule separated by at least three bonds. The force field parameters are available as public domain in their homepage [38]. In addition to the original parameter set 'ff94: parm94.dat' [34], much improved parameter set 'ff99: parm99.dat' [36] can be found in the homepage [38] for the use with Eq. (10).

In order to improve the accuracy for highly strained molecules and for fitting vibrational frequencies, Wang et al. [36] introduced the polarizable dipoles in addition to Eq. (10) as

$$E_{total} = E_{pair} + E_{pol} \qquad (11)$$

Later, Cieplak et al. (2001) [37] modified the polarizable version by polarizable dipoles attached to the atoms.

$$E_{pol} = -\frac{1}{2} \sum_i^i \alpha_i E_i^0 \cdot E_i , \qquad (12)$$

where α_i is the isotropic polarizability of ith atom, E_i is the electrostatic field on atom i due to all other charges and induced dipoles, and E_i^0 is the electrostatic field on atom ith due to permanent atomic charges only. There are no polarizabilities assigned to the "lone pairs". Here, the electrostatic field that induces dipole moment on ith atom is calculated self-consistently in an iterative way. The employed force field was the same as Wang et al. [36] and the complete parameter set, 'ff02: parm99.dat' is listed in [38]. Another variation is the polarizable force field with extra points on which additional point charges are located [35].

The molecular dynamics simulation code also called AMBER implementing these force fields is also developed by Kollman's group [38-40]. The recent version of this commercial code, AMBER 7 can handle SPC/E, TIP4P and OPLS potentials [38, 40].

IV. Many-body potential for carbon and silicon

The pair potential approximation cannot be assumed for atoms with covalent chemical bond such as silicon and carbon. The SW potential for a silicon crystal proposed by Stillinger and Weber in [41] consists of a two-body term and a three-body term that stabilizes the diamond structure of silicon. This original potential is still widely used because it accurately describes elastic properties, phonon dispersion relations, yield strength, and thermal expansion coefficients. Tersoff [42, 43] proposed a many-body potential function for silicon, carbon, germanium and combinations of these atoms. For simulations of solid silicon, this Tersoff potential [44] is widely used. Brenner modified the Tersoff potential for carbon and extended it for a hydrocarbon system [45]. A simplified form of Brenner potential removing rather

complicated 'conjugate terms' is widely used for studies of fullerene [46, 47] and carbon-nanotube. Both Tersoff potential and the simplified Brenner potential can be expressed as following in a unified form [3]. The total potential energy of a system is expressed as the sum of every chemical bond as

$$\Phi = \sum_{i} \sum_{j(i<j)} f_C(r_{ij}) \left\{ V_R(r_{ij}) - b_{ij}^* V_A(r_{ij}) \right\}, \quad (13)$$

where the summation is for every chemical bond. $V_R(r)$ and $V_A(r)$ are repulsive and attractive parts of the Morse type potential, respectively.

$$V_R(r) = f_C(r) \frac{D_e}{S-1} \exp\left\{-\beta\sqrt{2S}(r - R_e)\right\} \quad (14)$$

$$V_A(r) = f_C(r) \frac{D_e S}{S-1} \exp\left\{-\beta\sqrt{2/S}(r - R_e)\right\} \quad (15)$$

The cutoff function $f_C(r)$ is a simple decaying function centered at $r = R$ with the half width of D.

$$f_C(r) = \begin{cases} 1 & (r < R-D) \\ \frac{1}{2} - \frac{1}{2}\sin\left[\frac{\pi}{2}(r-R)/D\right] & (R-D < r < R+D) \\ 0 & (r > R+D) \end{cases}$$

$$(16)$$

Finally, b_{ij}^* term expresses the modification of the attractive force $V_A(r)$ depending on θ_{ijk}, the bond angle between bonds i-j and i-k.

$$b_{ij}^* = \frac{b_{ij} + b_{ji}}{2} \quad b_{ij} = \left(1 + a^n \left\{ \sum_{k(\neq i,j)} f_C(r_{ik}) g(\theta_{ijk}) \right\}^n \right)^{-\delta}$$

$$(17)$$

$$g(\theta) = 1 + \frac{c^2}{d^2} - \frac{c^2}{d^2 + (h - \cos\theta)^2} \quad (18)$$

Parameter constants for the Tersoff potential for silicon (improved elastic properties) [43] and carbon and for the Brenner potential for carbon are listed in Table 4. For a fuller discussion, see reference [3]. The original version of the Brenner code is available in his homepage [48].

Recently, a modified 'second generation empirical

bond order potential' has been developed by Brenner et al. [49]. A significantly better description of bond energies, lengths, and force constants as well as elastic properties is achieved with a single parameter set, even though the functions are rather complicated.

V. Pair potential and embedded atom method (EAM) for solid metal

For perfect solid metal crystals, several physical properties can be used to fit to the pair potential functions such as the Morse potential and Johnson potentials. The More potential is expressed as

$$\phi(r) = D_e \left[\exp\{-2\beta(r - R_e)\} - 2\exp\{-\beta(r - R_e)\} \right] \quad (19)$$

where D_e, R_e and β are dissociation energy, equilibrium bond length and a constant with dimensions of reciprocal distance, respectively. This form in Eq. (19) is corresponding to the special case of S = 2 in the generalized Morse-type functions in Eq. (14) and (15). The parameters calculated by Girifalco & Weizer [50] with energy of vaporization, the lattice constant and the compressibility for cubic metals (fcc and bcc) are listed in Table 5. The potential shapes are illustrated in Fig. 4 for several metal atoms. The reasonable elastic constants can be obtained by such fit [50].

For calculations of solid metals and alloys, the pair potential functions are not satisfactory when system is not perfectly uniform [51]. When some defect, surface and interfaces are included, pair potential functions with no term dependent on coordination cannot reproduce the realistic potential field. The angle dependence of potential is, in general, not as critical as the covalent cases such as carbon and silicon because d-orbital electrons are a little more flexible. In contrast to the "bond order concept" for covalent atoms, the use of the Embedded Atom Method (EAM) was suggested and developed by Daw and Baskes [52-55] as a way to overcome the main problem with two-body potentials. Later, the Modified Embedded Atom Method (MEAM) was also developed by Baske's group [56-59]. Here, the bond-angle was explicitly handled and the extension of the application range to covalent systems such as silicon was explored. Before introducing these potentials, it

Table 4 Parameters for Tersoff potential and Brenner potential.

	Tersoff (Si)	Tersoff (C)	Brenner (C)
D_e [eV]	2.6660	5.1644	6.325

R_e [nm]	0.2295	0.1447	0.1315
S	1.4316	1.5769	1.29
β [nm^{-1}]	14.656	19.640	1.5
A	1.1000×10^{-6}	1.5724×10^{-7}	1.1304×10^{-2}
N	7.8734×10^{-1}	7.2751×10^{-1}	1
δ	1/(2n)	1/(2n)	0.80469
c	1.0039×10^{5}	3.8049×10^{4}	19
d	1.6217×10^{1}	4.384	2.5
h	-5.9825×10^{-1}	-5.7058×10^{-1}	-1
R [nm]	0.285	0.195	0.185
D [nm]	0.015	0.015	0.015

Table 5 Morse potential parameters for cubic metals.

| Metal	β [nm^{-1}]	R_e [nm]	D_e [eV]
Pb	11.836	0.3733	0.2348
Ag	13.690	0.3115	0.3323
Ni	14.199	0.2780	0.4205
Cu	13.588	0.2866	0.3429
Al	11.646	0.3253	0.2703
Ca	8.0535	0.4569	0.1623
Sr	7.3776	0.4988	0.1513
Mo	15.079	0.2976	0.8032
W	14.116	0.3032	0.9906
Cr	15.721	0.2754	0.4414
Fe	13.885	0.2845	0.4174
Ba	6.5698	0.5373	0.1416
K	4.9767	0.6369	0.05424
Na	5.8993	0.5336	0.06334
Cs	4.1569	0.7557	0.04485
Rb	4.2981	0.7207	0.04644

should be noted that ideas of electron density and density functional theory (DFT) are discussed in the following formulation of the EAM and MEAM; however, they are classical potential functions and no quantum dynamic equation is solved when using the potential functions.

Ideas from the density functional theory (DFT) or the tight binding formalism lead to the following form for the total potential energy:

$$E_{total} = \sum_i F_i(\rho_{h,i}) + \frac{1}{2} \sum_i \sum_{j(\neq i)} \phi_{ij}(R_{ij}) \qquad (20)$$

Here, $\rho_{h,i}$ is the host electron density at atom i due to the remaining atoms of the system, $F_i(\rho)$ is the energy (gain) to embed atom i into the background electron density ρ, and $\phi_{ij}(R_{ij})$ is the core-core pair repulsion between atoms i and j separated by the distance R_{ij}. The electron density is approximated by the superposition of atomic densities as
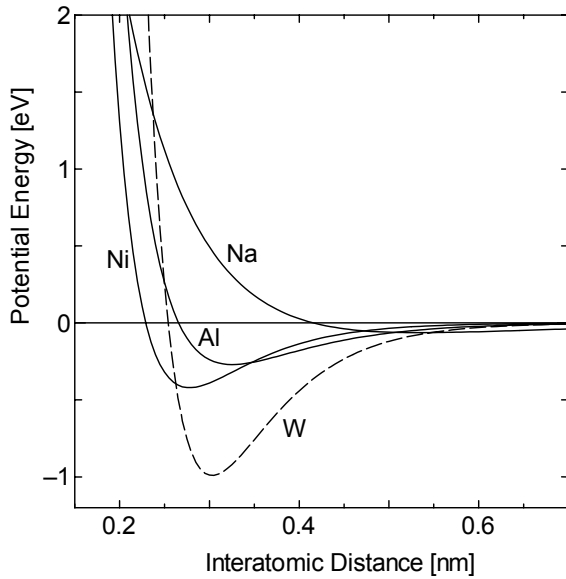
Figure 4 Morse potential for several solid metal atoms.

$$\rho_{h,i} = \sum_{j(\neq i)} \rho_j{}^a (R_{ij}) \qquad (21)$$

where $\rho_j{}^a(R)$ is the electron density contributed by atom j. With this approximation for the electron density, the actual computations using this method do not require more work than the use of pair interaction model. Note that the embedding function $F_i(\rho)$ only depends on the element of atom i, and does not depend on the source of the background electron density. Thus the same embedding function is used to calculate the energy of an atom in an alloy that is used in the pure material. The atomic electron density is computed from the Hartree-Fock wave function by

$$\rho^a(R) = n_s \rho_s(R) + n_d \rho_d(R), \qquad (22)$$

where n_s and n_d are the number of outer s and d electrons and $\rho_s(R)$ and $\rho_d(R)$ are the densities associated with the s and d wave functions. The spherically average s-like density $\rho_s(r)$ is calculated from Clementi [60] as

$$\rho_s(r) = \left| \sum_i C_i R_i(r) \right|^2 / 4\pi \qquad (23)$$

$$R_i(r) = \frac{(2\varsigma_i)^{(n_i+1/2)}}{\sqrt{(2n_i)!}} r^{n_i-1} e^{-\varsigma_i r}. \qquad (24)$$

And, $\rho_d(r)$ has the similar function. See Table V in Daw-Baskes [53] for an example of parameters. Hence, with

parametric values of n_s and n_d, $\rho_{h,j}$ in Eq. (21) can be calculated from the surrounding atom configurations. The fit parameter value of n_s is listed in Table 6 [54] and n_d is obtained by $Z_0 = n_s + n_d$.

The strategy to determine $F(\rho)$ and the pair repulsive form $\phi(R)$ is different from versions of EAM. According to Foiles et al. [54], the pair repulsive form is initially determined and $F(\rho)$ is determined by the comparison with the universal energy law [61].

The pair repulsive interaction between atoms of types A and B in terms of effective charges are expressed as

$$\phi_{AB}(R) = Z_A(R)Z_B(R)/R . \qquad (25)$$

And, the effective charge $Z(R)$ is assumed to be

$$Z(R) = Z_0 \left(1 + \beta R^\nu \right) e^{-\alpha R} \qquad (26)$$

with parameters listed in Table 6.

The universal energy law proposed by Rose et al. [61] is that the sublimation energy of most metals as a function of lattice constant as

$$E(a) = -E_{sub}(1 + a^*)e^{-a^*} \qquad (27)$$

where E_{sub} is the absolute sublimation energy at zero temperature and pressure. The quantity a^* is a measure of the deviation from the equilibrium lattice constant,

$$a^* = \frac{(a/a_0 - 1)}{\sqrt{E_{sub}/9B\Omega}} . \qquad (28)$$

Here, B is the bulk modulus of material, a is the lattice constant, a_0 is the equilibrium lattice constant, and Ω is the equilibrium volume per atom.

Again, the procedure to obtain F(ρ) form by Foiles et al. (1986) [54] is as follows.

(a) Assuming a perfect crystal, obtain the pair repulsive term $\phi(R)$ through Eq. (25).

(b) Calculate $\rho_{h,i}$ from Eq. (21).

(c) Make up F(ρ) function so that the energy in Eq. (20) represents the universal energy function in Eq. (27).

After determining the functional form of F(ρ), molecular dynamics calculations are not much morecomplicated compared with those carried out using pair potential functions. Functions of $F(\rho)$ and $Z(R)$ for various metal atoms can be found in several web sites as numerical tables.

Table 6 Some physical properties and parameters in embedded atom method [54].

	Cu	Ag	Au	Ni	Pd	Pt
a_0 (nm)	0.3615	0.409	0.408	0.352	0.389	0.392
E_{sub} (eV)	3.54	2.85	3.93	4.45	3.91	5.77
B (ergs/cm^3)	1.38	1.04	1.67	1.804	1.95	2.83
Atomic Configuration	$3d^{10}4s^1$	$4d^95s^2$	$5d^{10}6s^1$	$3d^84s^2$	$4d^95s^1$	$5d^96s^1$
Z_0	11	11	11	10	10	10
α	1.7227	2.1395	1.4475	1.8633	1.2950	1.2663
β	0.1609	1.3529	0.1269	0.8957	0.0595	0.1305
ν	2	2	2	1	1	1
n_s	1.000	1.6760	1.0809	1.5166	0.8478	1.0571

$Z_0 = n_s + n_d$

Finally, it should be noted that solid metal is always problematic for heat transfer problems because the lack of an effective technique of handling free electrons for heat conduction prevents a reasonable treatment of heat conduction through solid metal.

(c) Integration of the Newtonian equation

The integration of the equation of motion is straightforward. Unlike the simulation of fluid dynamics, a simpler integration scheme is usually preferred. Verlet's leap-frog method, as follows, is widely used in practical simulations [1]. After the velocity of each molecule is calculated as Eq. (29), positions are updated in Eq. (30).

$$\mathbf{v}_i\left(t+\frac{\Delta t}{2}\right) = \mathbf{v}_i\left(t-\frac{\Delta t}{2}\right) + \Delta t \frac{\mathbf{F}_i(t)}{m_i} \qquad (29)$$

$$\mathbf{r}_i(t+\Delta t) = \mathbf{r}_i(t) + \Delta t \mathbf{v}_i\left(t+\frac{\Delta t}{2}\right) \qquad (30)$$

A typical time step Δt is about 0.005 τ or 10 fs (1 fs = 1 femtosecond = 10^{-15}) with argon properties and the Lennard-Jones potential. More elaborate integration schemes such as Gear's predictor-corrector method [1] are sometimes employed depending on the complexity of the potential function and the demand of the accuracy of motion in each time step.

Even though the principal equation to solve is Eq. (1), classical rotational equations have to be solved for rigid small molecules with potentials such as the rigid water potential. The equation is the classical rotation equation of motion [1]. On the other hand, for large molecules expressed with potentials such as OPLS and the Amber potential need to be solved with the constraint dynamics, if the bond length is fixed. For such constraint dynamics, the efficient SHAKE algorithm [1] is often used.

(d) Boundary Condition: Spatial and Temporal

Scale

Since the spatial and temporal scale handled with the molecular dynamics method is extremely small compared to the scale of macroscopic heat transfer phenomena, the most important point of the design of a molecular dynamics simulation is the boundary condition. Many molecular dynamics simulations have used the fully periodic boundary condition, which assumes that the system is simply homogeneous for an infinite length scale. The implementation of the periodic boundary condition is very simple. Any information beyond a boundary can be calculated with a replica of molecules, as in Fig. 5. This boundary condition is usually used for two or four directions even for non-equilibrium calculations. The interaction of molecules is calculated beyond the periodic boundary with replica molecules. In order to avoid the calculation of potential between a molecule and its own replica, the potential must be cutoff to smaller than half the width of the base-cell scale. This is not a big problem for the short-range force such as Lennard-Jones potential, which decays as r^{-6}. Since Coulombic force decays only with r^{-1}, the simple cutoff is not possible. Usually, the well-known Ewald sum method [1] is employed, where the contribution from molecules in replica cells is approximated by a sophisticated manner. This is also somewhat of a problem for a system without the fully periodic conditions. The calculation of pressure using the virial theorem in Eq. (37) is also not straightforward. The stress tensor defined in a surface rather than the volume as in Eq. (37) is demonstrated to be better [62]. The definition of stress tensor is still being discussed [63].

Many problems in heat transfer may include a phenomenon with a larger scale than the calculation domain, such as instability or a large modulation of properties. The temperature and specific volume condition where the phase separation happens in a
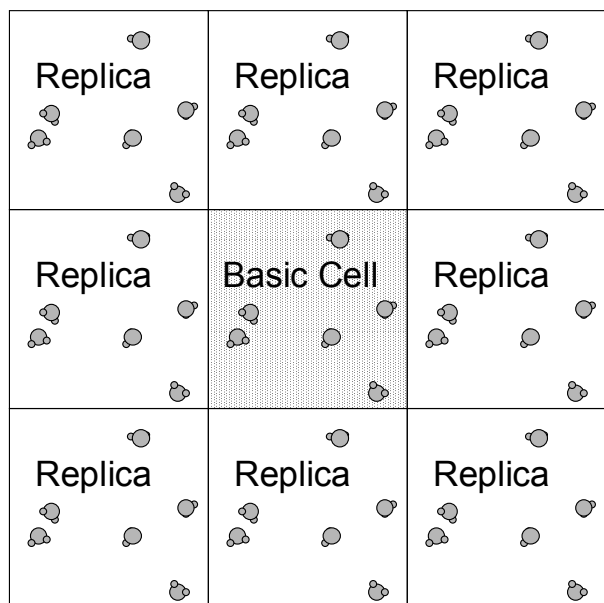
Figure 5 Two-dimensional image of periodic boundary condition.

macroscopic condition may be simulated as formation of a cluster in the small-scale calculation. Furthermore, for the non-equilibrium simulations, the establishment of the proper boundary condition is very difficult. In addition, the time scale that a molecular dynamics simulation can handle might be too short to simulate a slow dynamic process. The extreme example is the use of photon dynamics in heat conduction in solid materials as discussed in a later section.

The difficulty in the boundary condition is less for gas-phase molecules because the contribution of potential energy compared to kinetic energy is small. If the potential contribution is ignored, some simple boundary condition such as a mirror reflection boundary can be used, where simply changing the velocity component as if a molecule makes an inelastic reflection. There is no good boundary condition for a liquid system. When it is impossible to use the periodic boundary condition, a solid wall or a vapor layer can be connected in the realistic fashion. Then, the appearance of a new 'interface' leads to a very important change of the physics. Several different levels of the solid boundary conditions are discussed in detail in reference [3].

(e)   Initial condition and control of temperature and/or pressure

The initial condition for each molecule is usually assigned by giving the velocity

$$v = \sqrt{3 k_B T_C / m}$$

with random directions for all molecules for monatomic

molecules. The Maxwell-Boltzmann velocity distribution can be obtained after some equilibration calculations. The equilibrium system can often be calculated for constant temperature and constant pressure conditions. The simple temperature control of the equilibrium system can be realized by just scaling the velocity of molecules as

$$v_i' = v_i \sqrt{T_C / T}$$

with the current temperature T and the desired temperature T_C. More elaborate techniques to realize the constant temperature system are known as the Anderson method [64] and the Nosé-Hoover method [65, 66].

The Anderson method mimics random collisions with an imaginary heat bath particle. At intervals, the velocity of a randomly selected molecule is changed to a value chosen from the Maxwell-Boltzmann distribution. The choice of this interval is an important parameter.

The Nosé-Hoover thermostat method involve the modification of the equation of motion as

$$m_i \frac{d^2 \mathbf{r}_i}{dt^2} = \mathbf{F}_i - \zeta\, m_i \frac{d\mathbf{r}_i}{dt} \ , \ \frac{d\zeta}{dt} = \frac{2\left(E_k - E_k^{\ 0}\right)}{Q} \quad (31)$$

where ζ is the friction coefficient, E_k is kinetic energy of the system, $E_k^{\ 0}$ is kinetic energy corresponding to the desired temperature T_C, and Q is the thermal inertia parameter. All of these constant temperature techniques have been probed to give a statistically correct canonical ensemble, but the physical meaning of velocity re-scaling is not clear.

Andersen [64] described a technique to realize the constant pressure simulation. The simulation box size V is altered similar to the action of a piston with a mass. Parrinello and Rahman [67, 68] extended this technique to change the simulation box shape as well as size for solid crystal. Berendsen [69] proposed a very simple "pressure bath" technique for the constant pressure simulation. The system pressure obeys

$$dP / dt = (P_C - P) / t_P \quad (32)$$

by scaling the box size and position of molecules by a factor $\chi^{1/3}$ for each step.

$$\mathbf{r}' = \chi^{1/3} \mathbf{r} \ , \ \chi = 1 - \beta_T \frac{\Delta t}{t_p}\left(P_C - P\right) \quad (33)$$

where β_T, t_p are the isothermal compressibility and time constant parameter, respectively.

Finally, it should be stressed again that all of these techniques of constant temperature or constant pressure are artificial to reproduce the statistical ensemble and the physical meaning of the modification of position or velocity of each molecule is not clear.

(f) Thermophysical and dynamic properties

Molecular motion can be related to the thermodynamic properties through the entropy S defined as

$$S = k_B \ln \Omega \qquad (34)$$

where Ω is the phase-space volume. The statistical mechanical discussions for the microcanonical ensemble system (NVE ensemble), which is the 'molecular dynamics' ensemble, are fully described in Haile's textbook [2]. As the final result, the thermodynamics temperature for monatomic molecules is simply expressed as the kinetic energy of molecules.

$$T = \frac{1}{3Nk_B} \left\langle \sum_{i=1}^{N} m_i v_i^2 \right\rangle \qquad (35)$$

The internal energy is the total of the kinetic and potential energies, and pressure is defined through the virial theorem as follows.

$$U = \frac{3}{2} Nk_B T + \left\langle \sum_i \sum_{j>i} \phi(\mathbf{r}_{ij}) \right\rangle \qquad (36)$$

$$P = \frac{N}{V} k_B T - \frac{1}{3V} \left\langle \sum_i \sum_{j>i} \frac{\partial \phi}{\partial \mathbf{r}_{ij}} \cdot \mathbf{r}_{ij} \right\rangle \qquad (37)$$

There is no simple technique to measure entropy and free energy directly by the molecular dynamics method. They cannot be defined as the time averages of phase-space trajectories, but related to the phase-space volume as in Eq. (34) [2]. The thermodynamics integration or test particle method is employed [2]. These properties are often obtained by statistical Monte Carlo methods.

Even though the potential energy and pressure for a homogeneous fluid can be calculated for relatively small system, there is an important consideration for practical calculation. Since potential energy and pressure are affected from quite long-range volume, it is convenient to consider the potential cut-off corrections. The radial distribution function $g(r)$ is defined as

$$\rho g(r) = \frac{1}{N} \left\langle \sum_i^N \sum_{j \neq i}^N \delta \left[r - r_{ij} \right] \right\rangle \qquad (38)$$

This function means the number density of other

molecules within spheres with radii r and r + dr. Using this radial distribution function, the potential energy E_p for pair potential function can be expressed as.

$$\frac{E_p}{N} = 2\pi\rho \int_0^\infty \phi(r) g(r) r^2 dr \qquad (39)$$

The integration can be formally divided into the spherical region inside and outside of a sphere with the radius of the cut-off radius r_c of the potential function.

$$\frac{E_p}{N} = 2\pi\rho \int_0^{r_c} \phi(r) g(r) r^2 dr + 2\pi\rho \int_{r_c}^\infty \phi(r) g(r) r^2 dr \qquad (40)$$

$$\frac{E_p}{N} = \frac{\tilde{E}_p}{N} + E_{pLR} \qquad (41)$$

The first term in the right-hand side of Eq. (41) is the computed potential energy with the potential with cut-off distance r_c. The 2nd term in the right-hand side is the amount which should be corrected. Since the radial distribution function $g(r)$ tends to unity for large displacement r, the correction term is approximated to the integration form of only potential function as:

$$E_{pLR} \approx 2\pi\rho \int_{r_c}^\infty \phi(r) r^2 dr \qquad (42)$$

For Lennard-Jones potential, as an example, it can be analytically integrated as following.

$$E_{pLR}^* = \frac{8\pi\rho^*}{3(r_c^*)^3} \left(\frac{1}{3(r_c^*)^6} - 1 \right) \approx -\frac{8\pi\rho^*}{3(r_c^*)^3} \qquad (43)$$

Using this correction, molecular dynamics simulations using only 256 molecules of Lennard-Jones fluid can satisfactory reproduce the phase-diagram shown in Fig. 2.

A similar discussion is possible for the long-range correction term of pressure p_{LR}. The real pressure can be divided in the computed pressure $\tilde{p}$ and the long-range correction term p_{LR}.

$$p = \tilde{p} + p_{LR} \qquad (44)$$

The long-range correction term p_{LR} is expressed as

$$p_{LR} = -\frac{2}{3} \pi\rho^2 \int_{r_c}^\infty r \frac{d\phi(r)}{dr} g(r) r^2 dr \qquad (45)$$

For Lennard-Jones potential the integral leads to

$$p_{LR}^* = \frac{-16\pi\rho^{*2}}{3(r_c^*)^3}\left(1 - \frac{2}{3(r_c^*)^6}\right) \approx \frac{-16\pi\rho^{*2}}{3(r_c^*)^3}$$

$$(46)$$

Some dynamics properties such as self-diffusivity, thermal conductivity and viscosity can be calculated by the equilibrium simulations though the fluctuations of properties, assuming that the macroscopic concepts of the linear equations such as Fick's law or Fourier's law are valid. The definitions of the equations, statistical mechanical Green-Kubo formula and the practical formulas derived using the Einstein relations are listed in Table 7 [1, 2].


C. Molecular dynamics in microscale and nanoscale heat transfer

(a) Liquid-vapor interface

Surface tension is one of the benchmark properties to examine the applicability of the molecular dynamics method to the liquid-vapor interface and the potential function model. Detailed discussions are given in [3]. The typical simulation system is a liquid slab between vapor regions. When the liquid layer is thick enough, the bulk property of liquid can be obtained at the central region, and two liquid-vapor interfaces can be realized. Fig. 6 shows an example of such interface calculated with 8000 Lennard-Jones molecules. By taking a time average, the density profile, pressure tensor, and surface tension can be reasonably predicted. Though the normal pressure keeps a constant value, tangential pressure exhibits sharp drop near the liquid-vapor interface region. The integrated value of this tangential pressure drop is the surface tension. More, practically, surface tension in the interface can be calculated as

$$\gamma_{LG} = \int_{z_L}^{z_G} \left[P_N(z) - P_T(z)\right]dz \qquad (47)$$

The quite accurate prediction of surface tension has been demonstrated for Lennard-Jones fluid [70] and water [71] by integrating the difference of normal and tangential components of the pressure tensor across the surface. The other typical configuration is the liquid droplet surrounded by its vapor [3]. When the size of the droplet is large enough, the bulk property of liquid is expected at the central region. The well-known Young-Laplace equation relates the curvature of a liquid-vapor interface and surface tension to the pressure difference. Thompson et al. [72] used the spherical extension of Irving-Kirkwood's formula to

Table 7 Calculations of dynamic properties.
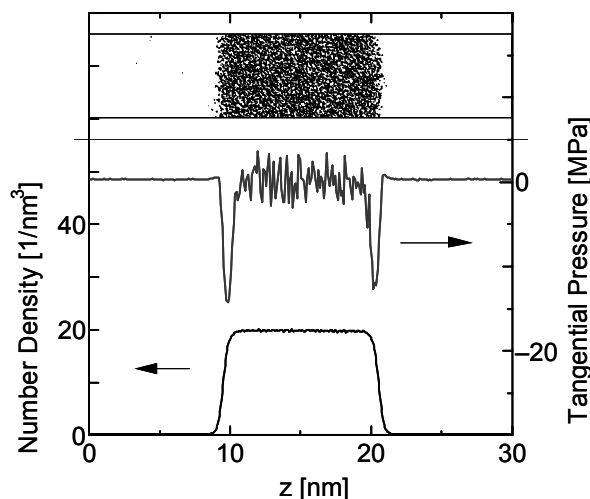
Figure 6 Density and tangential pressure distribution of a flat liquid-vapor interface (8000 argon molecules saturated at 99.5 K in 6×6×30 nm box).

calculate the normal pressure profile. The definition of the radius of a droplet is not straightforward, since the size of the droplet is normally very small and the liquid-vapor interface has a certain width. The equimolar dividing radius is one of the choice but more elaborate discussions based on the statistical mechanics are found in the literature (see references in [3]). Roughly a thousand molecules are enough to calculate the reasonable value of the bulk surface tension for argon. In the other extreme, the surface tension for very small clusters, which may be important in nucleation theory, would require some completely different approach, because such small clusters do not have the well-defined central liquid part assumed in the statistical mechanical discussions.

The determination of the condensation coefficient by molecular dynamics simulations is also very fascinating task. The condensation coefficient is defined as the ratio of the number of molecules condensing on the surface to the total number of molecules incident on the surface. Through the detailed studies of the liquid-vapor inter-phase phenomena of argon, water, and methanol, Matsumoto et al. [73, 74] pointed out that this macroscopic concept couldn't be directly converted to the molecular scale concept and that the 'molecular exchange' process must be considered. On the other hand, Tsuruta et al. [75] had reported a significant dependence of the trapping rate on the normal velocity of incident molecules.

A very recent example of molecular dynamics simulation of a liquid-vapor interface with the surfactant effect is shown in Fig. 7. Daiguji [76] simulated the effect of n-alcohols in the liquid-vapor interface of water and of LiBr solution. Here, three n-alcohols with different hydro-carbon chain length (n-propanol, C_3H_7OH; n-heptanol, $C_7H_{15}OH$; and

Property	Definition	Statistical Mechanical Green-Kubo Formula	With Einstein Relation For large t
Diffusion coefficient	$\dot{n} = -D\dfrac{\partial n}{\partial x}$	$\dfrac{1}{3}\displaystyle\int_0^\infty \langle \mathbf{v}_i(t)\cdot\mathbf{v}_i(0)\rangle dt$	$\dfrac{1}{6t}\langle |\mathbf{r}_i(t)-\mathbf{r}_i(0)|^2\rangle$
Thermal conductivity1	$q = -\lambda\dfrac{\partial T}{\partial x}$	$\dfrac{V}{k_B T^2}\displaystyle\int_0^\infty \langle \tilde{q}_\alpha(t)\cdot\tilde{q}_\alpha(0)\rangle dt$	N/A
Shear viscosity2	$F = \mu\dfrac{\partial U}{\partial y}$	$\dfrac{V}{k_B T}\displaystyle\int_0^\infty \langle \tilde{p}_{\alpha\beta}(t)\cdot\tilde{p}_{\alpha\beta}(0)\rangle dt$	$\dfrac{V}{k_B T 2t}\langle \left(\tilde{D}_{\alpha\beta}(t)-\tilde{D}_{\alpha\beta}(0)\right)^2\rangle$

$\tilde{q}_\alpha = \dfrac{d\delta\varepsilon_\alpha}{dt}$, $\delta\varepsilon_\alpha = \dfrac{1}{V}\sum_i r_{i\alpha}(\varepsilon_i - \langle\varepsilon_i\rangle)$, $\varepsilon_i = \dfrac{m_i v_i^2}{2} + \dfrac{1}{2}\sum_{j\neq i}\phi(r_{ij})$, $\alpha = x,\ y,\ z$

NVE only. $\tilde{p}_{\alpha\beta} = \dfrac{1}{V}\left(\sum_i m_i v_{i\alpha} v_{i\beta} + \sum_i\sum_{j>i} r_{ij\alpha} f_{ij\beta}\right)$, $\tilde{D}_{\alpha\beta} = \dfrac{1}{V}\sum_i r_{i\alpha} m_i v_{i\beta}$, $\alpha\beta = xy,\ yz,\ zx$

(a) $N_1 = 40$ (b) $N_1 = 60$ (c) $N_1 = 100$
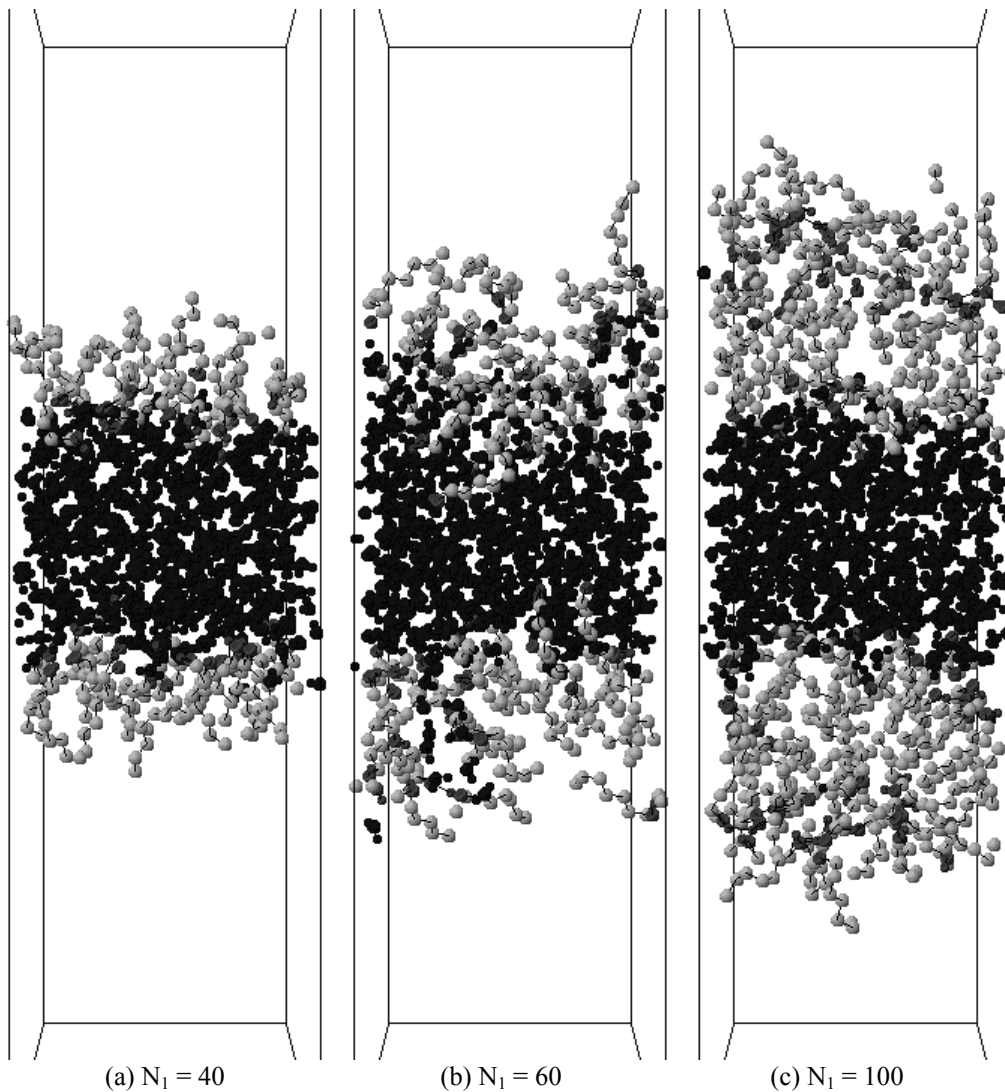
Figure 7 Snapshots of n-heptanol and water mixtures as the function of number of n-heptanol molecules, N_1 [11]. The Number of water molecules N_2 is 400. The dark molecules in the middle are water. Note the instability of water-alcohol interface is observed only at the medium concentration in (b).

n-undecanol, $C_{11}H_{23}OH$) were modeled with OPLS potential [21] and water was modeled with the popular SPC/E potential [19]. Only for the moderate length alcohol, n-heptanol, the instability of the interface was

observed for certain concentration as shown in Fig.7. When the alcohol concentration was lower as in Fig. 7(a), a monolayer of alcohol molecules with their hydrophilic side heading to water was stable. On the other hand, the 2-layers of alcohol molecules could be stable with the hydrophilic and hydrophobic interaction of 2-layers as in Fig. 7(c). With the medium concentration in Fig. 7(b), it seems that the alcohol molecules seek for more hydrophilic interaction with water molecules by creating the disturbance in the surface. Daiguji [76] further analyzed these phenomena from the thermodynamics standpoint and addressed the connection to the onset of Marangoni instability.

(b) Solid-liquid-vapor interactions

I. Lennard-Jones model system

Solid-liquid-vapor interaction phenomena have a very important role in phase-change heat transfer. The importance of the liquid wettability to the surface is apparent in a dropwise condensation, high-heat-flux boiling heat transfer and capillary liquid film evaporators. There are good reviews of the connection between microscopic and macroscopic views of the wetting phenomena by Dussan [77], and from a slightly more microscopic point of view by Koplik and Banavar [78]. Furthermore, amolecular dynamics treatment of asimple Lennard-Jones liquid droplet on the solid surface and Lennard-Jones vapor bubble on the solid surface are discussed in [3]. In brief, except for the two or three liquid layers near the surface, the averaged shape of the Lennard-Jones liquid droplet is close to the semi-spherical as shown in Fig. 8. A snapshot of a droplet on the solid surface and the 2D density distribution are compared in Fig. 8 [79-81]. By fitting a circle to the density contour disregarding a few layers of liquid near the solid surface, "contact angle" can be measured. The effect of the interaction potential on the shape of the liquid droplet is apparent in Fig. 9 [79-81]. With increase in the strength of the interaction potential between the surface molecule and argon, the flatter shape is observed. In contrast, the shapes of vapor bubble in liquid are shown in Fig. 10 [81, 82]. The cosine of measured contact is linearly dependent on the strength of the surface potential as in Fig. 11 [81]. Here, as the measure of the strength of the interaction, the depth of the integrated potential

$$\varepsilon_{SURF} = (4\sqrt{3}\pi / 5)(\sigma_{INT}^2 / R_0^2)\varepsilon_{INT} \qquad (48)$$

was employed [3]. The controversial discussions whether the Young's equation can hold or not in such a system has been widely discussed in the past (see

references in [3]). However, at least the concept of surface energy balance should be valid. For the macroscopic contact, the well-known Young's equation relates the contact angle to the balance of surface energies as

$$\cos\theta = \frac{\gamma_{SG} - \gamma_{SL}}{\gamma_{LG}} \qquad (49)$$

where γ_{SG}, γ_{SL} and γ_{LG} are surface energies between solid-gas, solid-liquid, and liquid-gas, respectively. With a change in the energy parameter between liquid and solid molecules, γ_{LG} is kept constant and γ_{SG} does not change much compared with γ_{SL} because the vapor density is much lower compared with liquid density. With increase in ε_{SURF}, γ_{SL} should decrease almost proportionally because of the gain in potential energy in the liquid-solid interface. Then, (γ_{SG} - γ_{SL}) should increase and the Young's equation predicts the increase in $\cos\theta$. Hence, the linear relation in Fig. 11 can be roughly explained by the analogy with Young's equation.

Here, an idea of the evaluation of the asymptotic macroscopic contact angle is introduced. Since the thickness and the extension of the layered structure near the surface are scaled with the molecule diameter (only up to about 5 molecular layers), the importance of this structure should vanish for a large enough liquid droplet except for the modification of the liquid-solid surface energy γ_{LS}. The size dependence of the contact angle is shown in Fig. 12. By using the one-dimensional potential to represent the surface, up to $N = 32000$ system was calculated for the interaction potential parameters nearly equivalent to E4 in Table 8. With increase in the number of liquid molecules N_L of a droplet, the gradual decrease of $\cos\theta$ (increase of contact angle) was observed. Let's assume that the extended liquid layer near the surface is the primary factor of this size dependence. The extension of the liquid layer causes the increase of liquid-solid interface. Hence, this increase of the liquid-solid interface area is equivalent to the decrease of γ_{SL} (potential energy gain by liquid-solid interface reduces the surface energy), increase in (γ_{SG} - γ_{SL}), and hence, increase in $\cos\theta$ by Eq. (49). Assuming that the extension of the first liquid layer is constant irrespective to the size of the droplet, the following dependence of contact angle on the number of liquid molecules N_L can be derived.

$$\cos\theta = \cos\theta_\infty \frac{\left(N_L^{1/3} + \Delta r\right)^2}{N_L^{2/3}} \qquad (50)$$

(a) snapshot
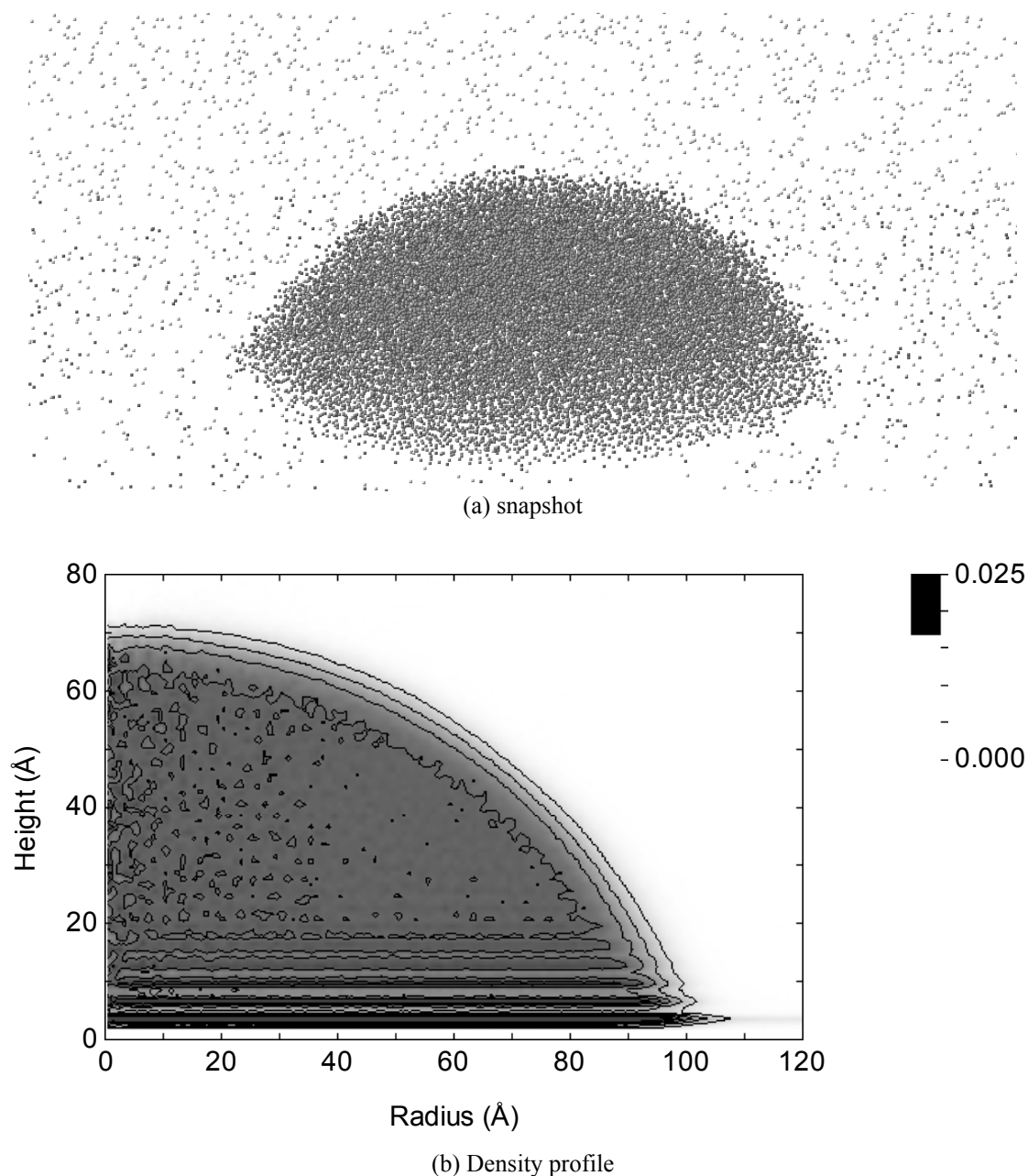
(b) Density profile

Figure 8 A snapshot of a liquid droplet on solid surface compared with the two-dimensional density profile: 32000 Lennard-Jones molecules on a surface.

where θ_∞ is an asymptotic contact angle for macroscopic system, $N_L^{1/3}$ is proportional to the radius of the liquid-solid contact surface, and Δr is the parameter related to the extension of the interface. The solid line in Fig. 12 is the least-square fit with Eq. (50): $\cos\theta_\infty = 0.35$, $\Delta r = 2.72$. This Δr corresponds to about 9.2 Å, and agrees well with the observation of the extended first layer length in Fig. 8. Hence a possible connection to the macroscopic system is quite successful for this system.

II. Water droplet on a platinum solid surface

As a more practical simulation of solid-liquid-vapor interaction, a water droplet on a platinum solid surface is shown in Fig. 13 [83]. Water molecules were modeled with the SPC/E potential [19]. The interaction potential between water and platinum molecules was expressed by the potential function developed by Zhu and Philpott [84], based on the extended Hückel calculations. The potential function consists of water molecule-conduction electron potential, anisotropic short-range potential and isotropic short-range r^{-10} potential as follows.
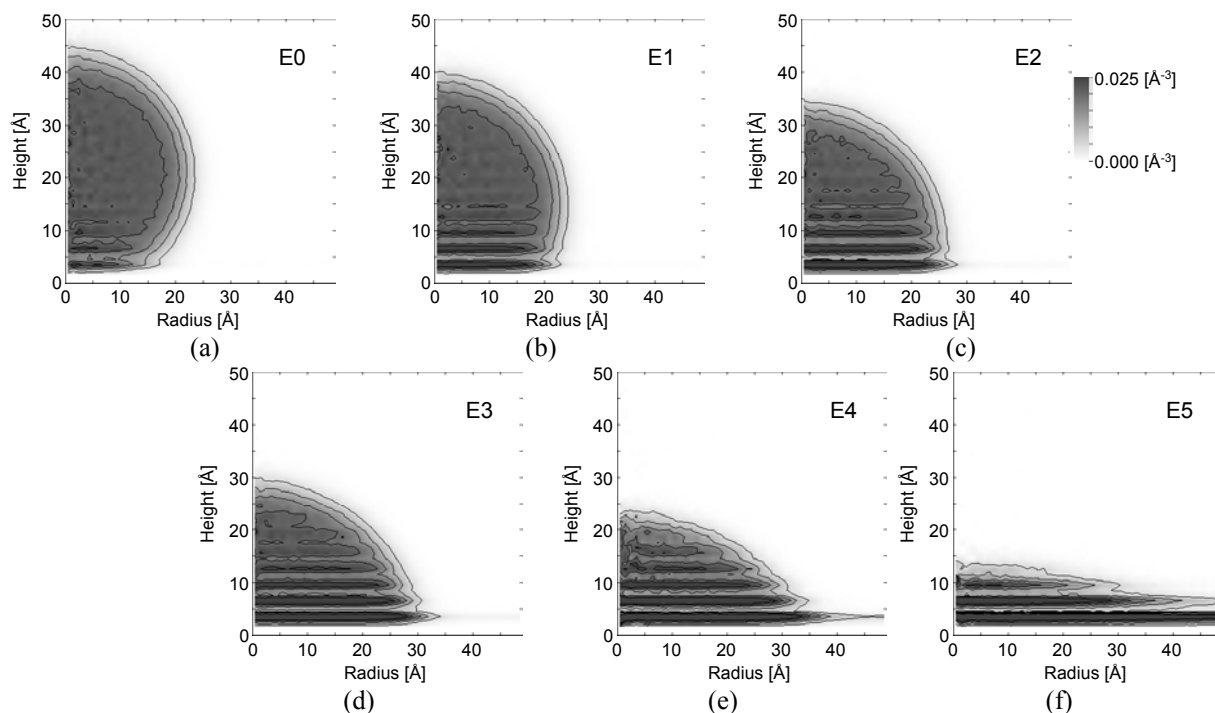
Figure 9 Two dimensional density distributions for a Lennard-Jones liquid droplet. See Table 8 for interaction parameters.
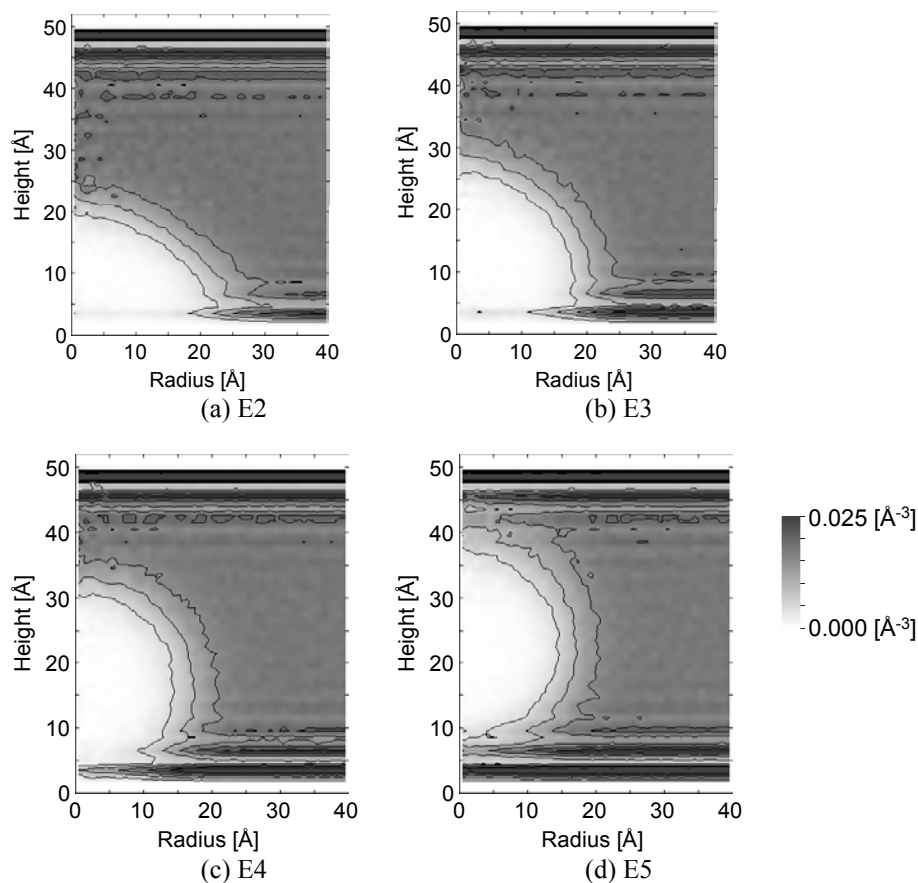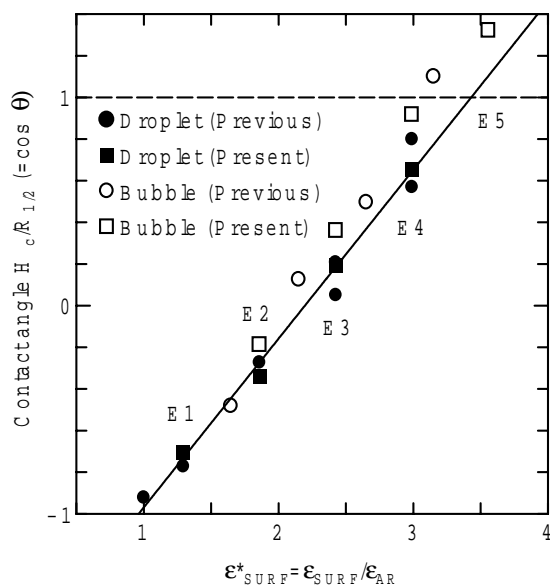

Figure 10 Two dimensional density distributions for Lennard-Jones bubble. See table 8 for interaction parameters.

Table 8 Calculation conditions of contact of Lennard-Jones fluid.

		Droplet		Bubble	
	ε^*_{SURF}	ε_{INT} [10^{-21}J]	θ [deg]	ε_{INT} [10^{-21}J]	θ [deg]
E0	0.73	0.228	-	-	-
E1	1.29	0.404	135	-	-
E2	1.86	0.581	110	0.527	101
E3	2.43	0.758	79	0.688	69
E4	2.99	0.935	49	0.848	23
E5	3.56	1.112	-	1.009	-

Figure 11 Dependence of contact angle on the integrated depth of surface potential ε_{SURF}.
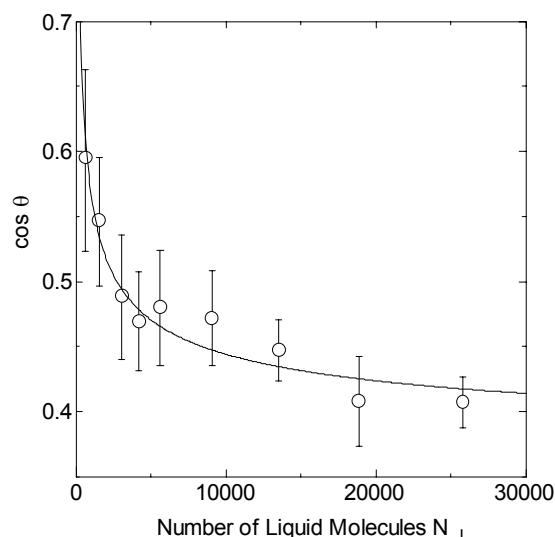
Figure 12 Size dependence of calculated contact angle.

$$\phi_{H_2O-surf} = \phi_{H2O-cond} + \phi_{an}(O;\mathbf{r}_O) + \phi_{isr}(O;\mathbf{r}_O)$$

$$+ \sum_H \left[\phi_{an}(H;\mathbf{r}_H) + \phi_{isr}(H;\mathbf{r}_H) \right] \quad (51)$$

$$\phi_{H2O-cond} = \sum_{l,k} \frac{q_l q_k}{2r_{lk}} \quad (52)$$

$$\phi_{an}(p;\mathbf{r}_p) = 4\varepsilon_{p-Pt} \sum_j \left[\left(\frac{\sigma_{p-Pt}^2}{(\alpha\rho_{pj})^2 + z_{pj}^2} \right)^6 \right.$$

$$\left. - \left(\frac{\sigma_{p-Pt}^2}{(\rho_{pj}/\alpha)^2 + z_{pj}^2} \right)^3 \right] \quad (53)$$

$$\phi_{isr}(p;\mathbf{r}_p) = -4\varepsilon_{p-Pt} \sum_j \frac{c_{p-Pt}\sigma_{p-Pt}^{10}}{r_{pj}^{10}} \quad (54)$$

where $\alpha = 0.8$, $\sigma_{O-Pt} = 0.270$ nm, $\varepsilon_{O-Pt} = 6.44 \times 10$-21 J, $c_{O-Pt} = 1.28$, $\sigma_{H-Pt} = 0.255$ nm, $\varepsilon_{H-Pt} = 3.91 \times 10^{-21}$ J, $c_{H-Pt} = 1.2$. Here, Eq. (52) represents Coulomb potential between point charge of water molecule and its image charge located at symmetrical position below the image plane. This potential takes the minimum value when a water molecule sits on top of a platinum atom heading hydrogen atoms upward. The contact structure of the water droplet with a finite contact angle on the absorbed monolayer water film in Fig. 13 was quite a surprise. It was the first demonstration of such a structure with equilibrium molecular dynamics simulation. Even though the existence of a thin liquid film is sometimes assumed in the liquid-solid contact theories, the simple energy consideration using the Young's equation should conclude that the water droplet should be very much wettable to a water film. However, the contact angle is determined by the surface energy between this monolayer water film and bulk liquid water. The monolayer film does not have the characteristics of bulk water. It has quite high density due to the strong interaction to the platinum surface atoms, and the interaction of this film with normal water strongly depends on the density of the film. A higher density of the water monolayer results the lower interaction. With this assumption, the clear dependence of contact angle on the platinum crystal lattice structure can also be explained [83].
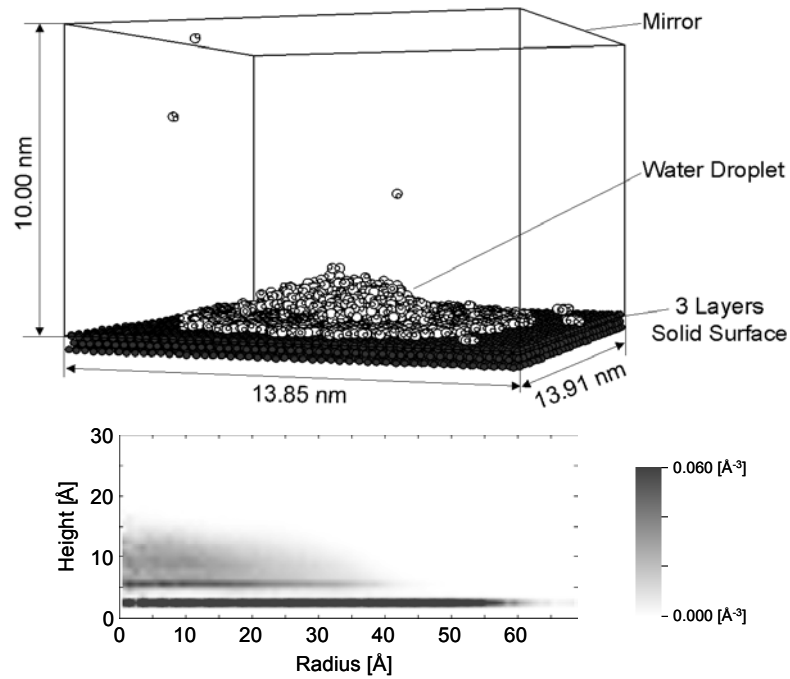
Figure 13 A snapshot and 2-dimensional density profile of an equilibrium water droplet on a platinum surface at 350K. SPC/E water molecules were interacting with the harmonic platinum surface represented by 3 layers of (111) surface through the water-platinum potential proposed by Zhu-Philpott.
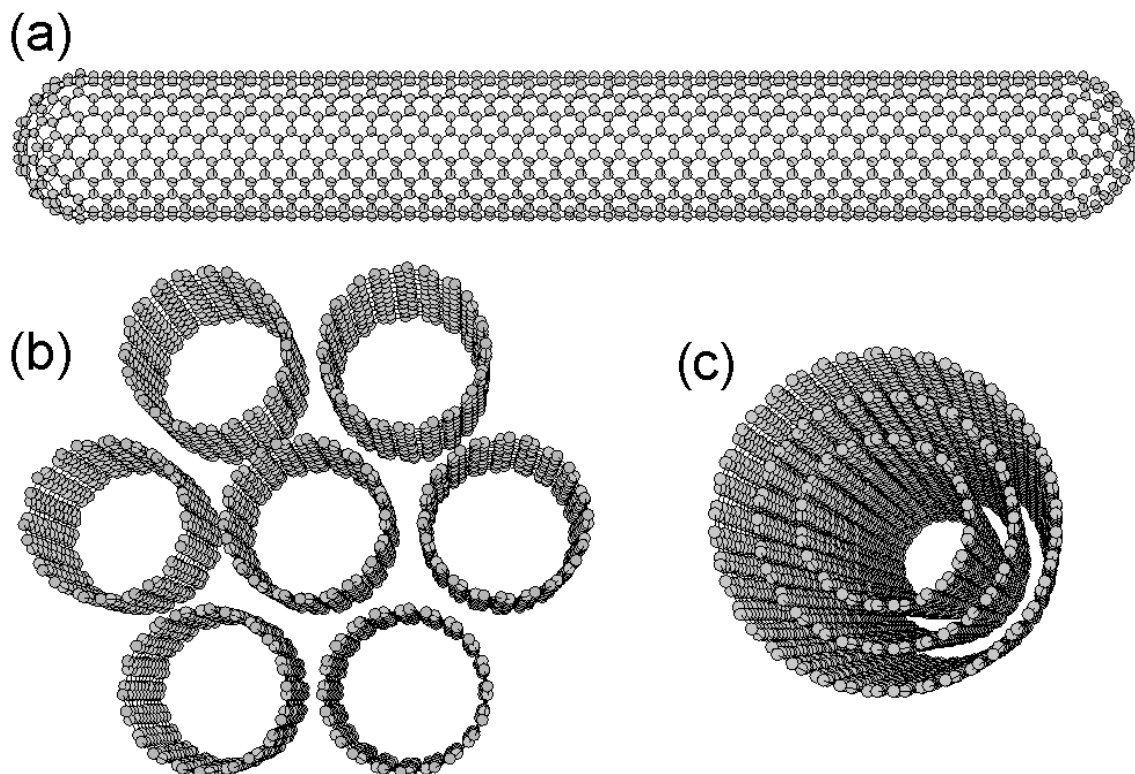
Figure 14 Geometrical structure of carbon nanotubes. (a) Single-walled carbon nanotube (SWNT) with (10, 10) chirality. (b) A bundle of SWNTs. (c) Multi-walled carbon nanotube (MWNT).

(c) Interaction of fluids with carbon nanotubes

I. Introduction of carbon nanotubes

The multi-walled carbon nanotubes (MWNTs) discovered by Iijima in [85] and especially single walled carbon nanotubes (SWNTs) [86] are regarded as the most important material in "nanotechnology." The structure of SWNTs and MWNTs are shown in Fig. 14. The geometry of SWNT can be described as a single layer of a graphite sheet that is rolled up into a cylinder. The diameter is only 0.7 nm to about 2 nm and the length is about a few microns. The geometry can be specified by the chiral vector

$$\mathbf{C}_h = n\mathbf{a}_1 + m\mathbf{a}_2 \equiv (n, m) \qquad (55)$$

where $\mathbf{a}_1$ and $\mathbf{a}_2$ are unit vectors of the honeycomb lattice of the graphite sheet. By rolling up so that 2 atoms at origin and at $\mathbf{C}_h$ in the honeycomb lattice will meet, $\mathbf{C}_h$ will be the circumference of the SWNT. Hence, the geometry of a SWNT is usually described by the chiral index (n, m). Details of properties of carbon nanotubes are describes in monographs [87, 88]. The electronic property of SWNT is most exciting that it may be metallic or semiconductor depending on chirality. Along with the superior mechanical strength and thermal conductivity, there are many possible applications such as ultimate electric wire, field effect transistor, field emitter for flat panel display, probe of scanning probe microscope, thermal device, reinforced material, gas absorption material.

Most of the studies of SWNTs have started after the discoveries of macroscopic generation techniques, the laser-furnace [89] method in 1996 and the arc-discharge [90] method in 1997. Recently, the bulk generation of SWNTs by the catalytic CVD process called HiPco [91] was developed. An alternative catalytic CVD method from alcohol was introduced by the author's group [92].

II. Hydrogen absorption with single-walled carbon nanotubes

Since the suggestion of high efficiency storage of hydrogen with SWNTs by Dillon et al. [93], experimental determinations of the storage capacity and mechanism of storage have been extensive. Hydrogen storage capacity of high purity SWNT was reported to be more than 8 wt % at 12 MPa and 80 K [94], or 4.2 wt % at 10 MPa at room temperature [95]. Recent experimental studies are concluding that the hydrogen storage capacity of SWNTs at room temperature is less than 1 wt % [96]. Most of molecular dynamics simulations have been consistently predicting the very low hydrogen storage capacity at room temperature [97, 98].

An example of molecular dynamics simulation of hydrogen absorption is shown in Fig. 15 [99]. Assuming the physical adsorption of hydrogen to the surface of carbon nanotubes, potential forms between H_2-H_2 and C-H_2 were both expressed by Lennard-Jones (12-6) functions, with parameters: ε_{HH} = 3.180 meV, σ_{HH} = 2.928 Å, ε_{HC} = 2.762 meV and σ_{HC} = 3.179 Å. Each nanotube was regarded as rigid molecule and van der Waals potential between nanotubes was derived as a Lennard-Jones (8-4) function by integrating potential function between carbon atoms. The potential energy has minimum at the interstitial sites (between nanotube), and has a low value at the endohedral sites (inside a nanotube). The interaction potential is too weak for the efficient hydrogen storage at room temperature for the use in fuel cell vehicles.
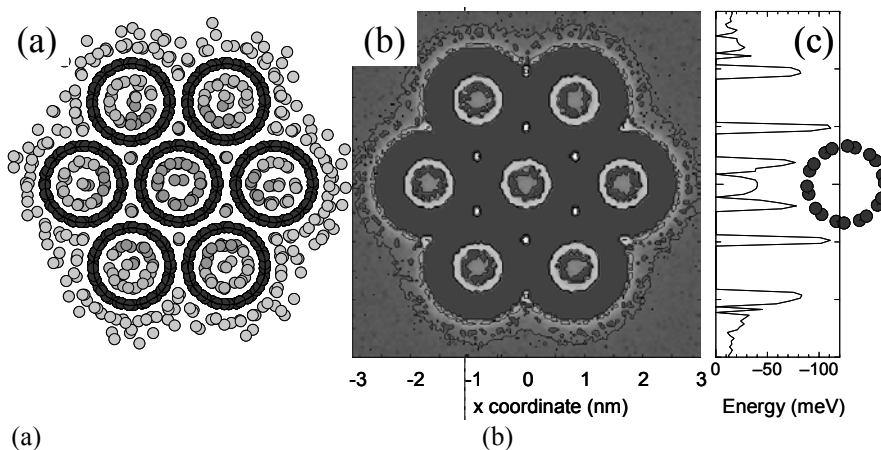
III. Water in carbon nanotubes

Some recent experimental work [100, 101] shows the existence of trapped aqueous solutions in MWNTs generated with a hydrothermal method. Even though the composition of this aqueous solution is unknown, the liquid and vapor interface structure and phase-change in the completely closed space of about 50 nm are truly exciting. The solution was quite wetting to the walls of carbon nanotubes. Another experimental work [102] suggest that liquids with a surface tension lower than 100-200 mNm^{-1} can wet carbon nanotubes, i.e. is expected that water, with a surface tension of 73 mNm^{-1}, should wet a carbon nanotube. Figure 16 shows a snapshot of water cluster in a SWNT with quite large diameter of 2.77 nm. The interaction potential between carbon and water is simply Lennard-Jones function between carbon and oxygen atom. The interaction parameters are ε_{OC} = 1.08×10^{-21} J and σ_{OC} = 0.316 nm. It is clearly seen that the water cluster is not so wetting but the potential energy is lower than in vacuum. Walther et al. [103, 104] studied the wetting phenomena of SWNTs in more detail by molecular dynamics simulations. In addition to the Lennard-Jones potential between oxygen and carbon, a quadrupole interaction between the carbon and the partial charges on hydrogen and oxygen atoms was also considered. The simulation results show that pure water does not wet the carbon nanotube. Just like graphite, the wall of nanotube is strongly hydrophobic.
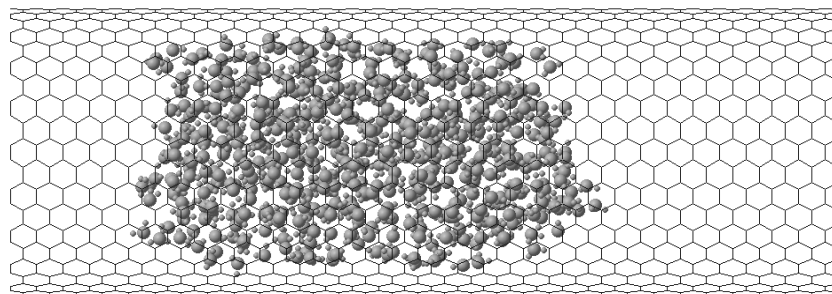
(d) Nucleation and phase change

I. Homogeneous nucleation

Homogeneous nucleation is one of the typical macroscopic phenomena directly affected by the

(a)

-3   -2   -1   0   1   2   3

x coordinate (nm)

Energy (meV)

0   −50   −100

(a)   (b)

Figure 15 Physisorption of hydrogen in a bundle of single-walled carbon nanotubes at 77K. (a) A snapshot, (b)(c) potential energy distribution.

Figure 16 Structure of water cluster in a carbon nanotube. (512 water molecules in (20, 20) nanotube with 2.77 nm diameter).

molecular scale dynamics. Recently, Yasuoka et al. have demonstrated the direct molecular dynamics simulations of the nucleation process for a Lennard-Jones fluid [105] and for water [106]. The key technique for such a calculation is the temperature control as discussed by Ikeshoji et al. [107] by observing the magic number clusters of 13, 19 and 23, which are abundantly observed in experimental mass spectra. After quenching to the supersaturation condition, the condensation latent heat must be removed for the successive condensation. Yasuoka et al. [105] used 5000 Lennard-Jones molecules for the simulation mixed with 5 000 soft-core carrier gas molecules connected to the Nosé-Hoover thermostat for the cooling agent. This cooling method mimicked the carrier gas of supersonic jet experiments. Through the detailed study of growth and delay of nuclei size distribution, they have estimated the nucleation rate and the critical size of nucleus. The nucleation rate was seven orders of magnitude larger than the prediction of classical nucleation theory. Their similar simulation [106] for water of TIP4P potential at 350 K resulted in a nucleation rate two orders of magnitude smaller than the classical nucleation theory, in good agreement with the "pulse expansion chamber" experimental results.

II. Heterogeneous nucleation

Heterogeneous nucleation is also practically important in most heat transfer problems. Fig. 17 shows an example of the heterogeneous nucleation of liquid droplet on a solid surface [108]. Argon vapor consisted of 5760 Lennard-Jones molecules was suddenly cooled by the solid wall controlled with the phantom technique [3]. The phantom molecules modeled the infinitely wide bulk solid kept at a constant temperature with proper heat conduction characteristics. The potential between argon and solid molecule was also represented by the Lennard-Jones potential function, and the energy scale parameter was changed to reproduce various wettabilities. After the equilibrium condition at 160 K was obtained, the temperature of the solid surface was suddenly set to 100 K or 80 K by the phantom molecule method. Initially, small clusters were appeared and disappeared randomly in space. Then larger clusters grew preferentially near the surface for wettable cases. On the other hand, for the less wettable condition, relatively large clusters grew without the help of surface just like the homogeneous nucleation. The nucleation rate and free energy needed for cluster formation were not much different from the prediction of the classical heterogeneous nucleation theory in case of smaller cooling rate.

A molecular dynamics simulation of homogeneous [109] or heterogeneous [82] nucleation of a vapor bubble is much more difficult compared to the nucleation of a liquid droplet. Even though the formation of a vapor bubble can be reproduced by expanding the liquid to a negative pressure, qualitative comparison of nucleation rate or critical radius is not easy.

III. Crystallization of amorphous silicon

An example of crystal growth process from amorphous silicon is shown in Fig. 18 [110]. By using the Tersoff (C) potential [44], the crystallization process was calculated With the solid phase epitaxy (SPE) configuration [e.g. 111], the crystal growth in (001) and (111) directions were compared. It was observed that growth in (111) direction was dominant in Si crystallization at the high temperature region possibly because of instability of (001) amorphous/crystal (a/c) interface. Then, the newly developed crystallization system that consisted of a Si cluster on an amorphous

surface with a small number of seed atoms was also simulated. With this configuration, the artifacts induced by the periodic boundary condition could be completely neglected. From the time profile of the Si crystal nuclei size, the classical critical nuclei size was estimated to be around 110 atoms.

IV. Formation of clusters, fullerene, and carbon nanotubes

The intermediate cluster structure are extremely important when some of them can be stably observed as the end products such as the simulation of fullerene formations [46, 47] and endohedral metallofullerene formations [112]. The formation mechanism of SWNTs is theoretically interesting and also extremely important for the development of large scale and controlled generation techniques. The molecular dynamics simulation [113] of laser-oven or arc-discharge processes is very much similar to the simulation of endohedral metallofullerene formation, because the

| (a) 500 ps | (b) 1000 ps | (c) 1500 ps |
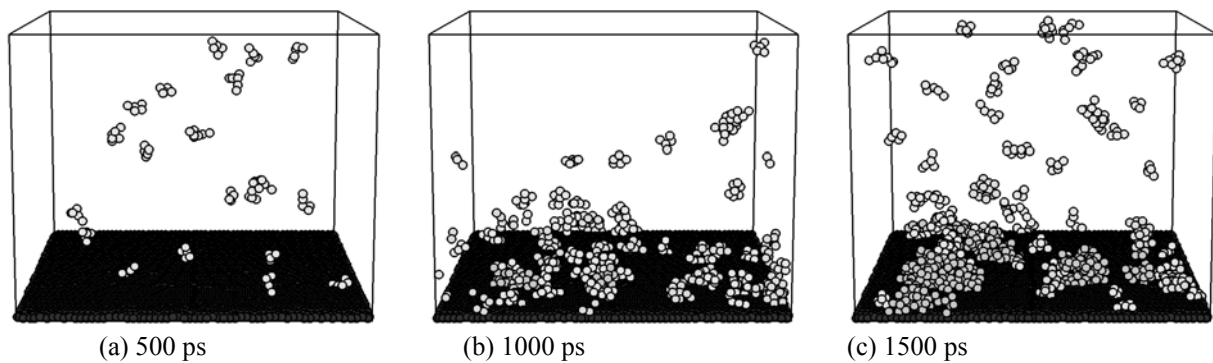
Figure 17 Nucleation of liquid droplet on a solid surface. Only clusters larger than 5 atoms are displayed for clarity.
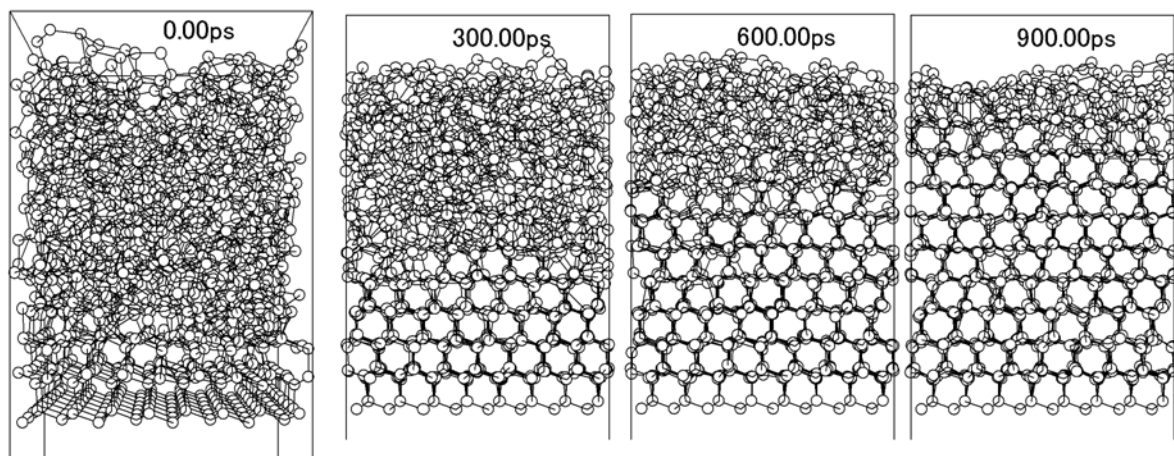

Figure 18 Snapshots of Solid Phase Epitaxy (SPE) growth of silicon crystal in (111) at 2100K.

actual experimental condition is almost the same except for the small amount of metal doped in the graphite

material. Recently, SWNTs formation mechanism for CVD techniques [91, 92, 114] is getting more attention

because they are expected to supply large amount of SWNTs at a lower cost. In HiPco process [91], a Fe metal cluster is formed by the decomposition of $Fe(CO)_5$ precursor molecule in the hot chamber. Then, high pressure CO makes the disproportional reaction on the metal cluster as

$$CO + CO \rightarrow CO_2 + C(solid) \qquad (56)$$
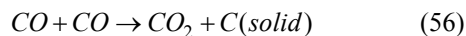
On the other hand, in a supported catalyst CVD process, hydrocarbon [114] or alcohol [92] will be decomposed on the catalytic metal cluster supported by silica, alumina, magnesia or zeolite. In both process, the carbon atom is supplied to the metal cluster in a high temperature condition. Fig. 19 shows the nucleation process of a SWNT in a catalytic CVD process [115]. Using the simplified Brenner [45] potential for carbon-carbon interaction and the empirical metal-carbon potential functions [112], the nucleation process of SWNT by successive collisions of hydrocarbon molecules to a metal cluster was simulated. At first, the initial Ni cluster structures of various sizes were obtained by annealing a FCC crystal at 2 ns in 2000K. As the initial condition of clustering process, the completely random vapor mixture of 500 carbon atoms and one of the Ni clusters obtained above were allocated in 20 nm cubic fully-periodic simulation cell. The interaction between isolated carbons was represented by the Lennard-Jones potential to avoid the generation of carbon clusters before the collision to the metal catalyst. Initially, carbon atoms melted into the metal cluster and made the carbon-metal binary cluster. With more supply of carbon atoms, some of carbon atoms precipitated out to the fullerene cap structure. It seems that the SWNT structure is being formed.

(e) Heat Conduction and heat transfer

The thermal conductivity of homogeneous material can be calculated by 3 different techniques of molecular dynamics: (1) equilibrium molecular dynamics with the Green-Kubo's formula, (2) non-equilibrium molecular dynamics (NEMD) developed by Evens [116, 117], and (3) Non-equilibrium molecular dynamics with direct temperature differences. It should be noted that (2) and (3) are both sometimes called non-equilibrium molecular dynamics. For the homogeneous system all of these simulations should give the same thermal conductivity with adequate simulation conditions [118, 119].

The simulation of heat conduction is not always the simple calculations of thermal conductivity. The validity of Fourier's law in an extremely microscopic system such as thin film can only be examined by the direct non-equilibrium heat conduction calculation. The mechanism of heat conduction itself is also interesting [120,121]. The heat flux through a volume is calculated as

$$\mathbf{q} = \frac{1}{2V}\left[\sum_i^N m_i v_i^2 \mathbf{v}_i + \sum_i^N \sum_{j \neq i}^N \phi_{ij} \mathbf{v}_i - \sum_i^N \sum_{j \neq i}^N \left(\mathbf{r}_{ij}\mathbf{f}_{ij}\right)\mathbf{v}_i\right]$$

$$(57)$$

where the first and second terms related to summations of kinetic and potential energy carried by a molecule *i*. The third term, the tensor product of vectors r_{ij} and f_{ij}, represents the energy transfer by the pressure work. Because of the third term, the calculation of heat flux is not trivial at all.

I. Thermal boundary resistance

An example of the spatial non-equilibrium simulation is shown in Fig. 20 [122]. The purpose of this simulation

Ni₁₀₈   ◯ Nickel

0 ns   20 ns   50 ns   100 ns   130 ns
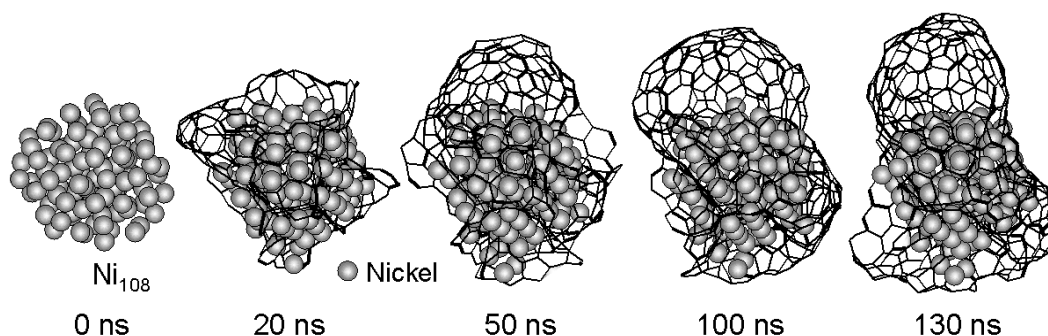
Figure 19 Growth simulation of single-walled carbon nanotubes from a catalytic metal clusters. Carbon atoms are not shown for clarity.
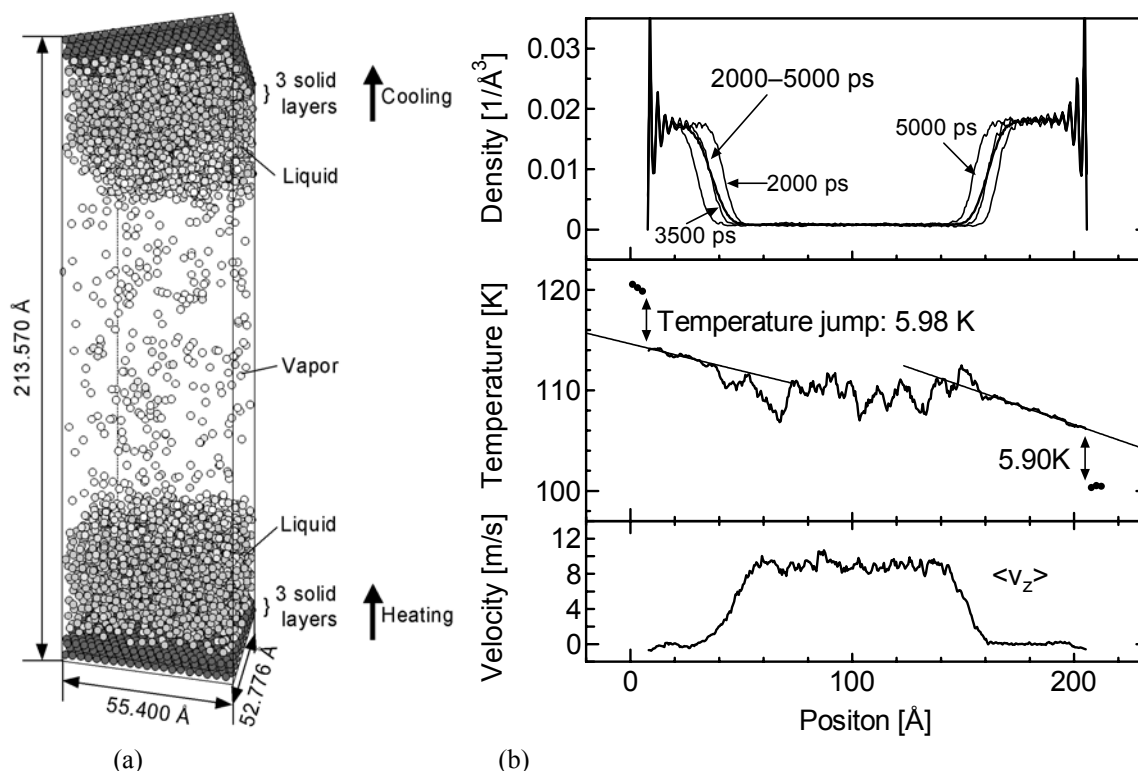
Figure 20 Non-equilibrium molecular dynamics for inter-phase heat transfer. (a) A snapshot, (b) density, temperature, and velocity distributions.

was to measure the thermal resistance in the interface of liquid and solid. A vapor region was sandwiched between liquid layers, which were in contact with two solid walls. While independently controlling temperatures at ends of walls by the phantom method [3], energy flux through the system was accuratelycalculated. The heat flux and vapor pressure became almost constant after about 2 ns after suddenly enforcing the temperature difference between the surfaces. The measured temperature distribution normal to interfaces in this quasi-steady condition shown in Fig. 20b revealed a distinctive temperature jump near the solid-liquid interface, which could be regarded as the thermal resistance over the interface. The temperature distribution in the liquid region (see the density profile in the top panel of Fig. 20b) can be fit to a linear line, and the thermal conductivity λ_L can be calculated from this gradient and heat flux $\dot{q}_w$ as $\lambda_L = \dot{q}_W /(\partial T / \partial z)$. This value was actually in good agreement with the macroscopic value of liquid argon. The thermal resistance R_T was determined from the temperature jump T_{JUMP} and the heat flux q_W as $R_T = T_{JUMP} /q_W$. This thermal resistance is equivalent to a liquid heat conduction layer of 5~20 nm thickness and hence, is important only for small systems.

The configuration in Fig. 20a seems to be used for the non-equilibrium condensation and evaporation studies since the condensation in the upper liquid-vapor interface and the evaporation in the lower interface are quasi-steady. The heat flux through higher temperature side q_W^{evap} was consumed for the latent heat of the evaporation, and the residual heat flux $\dot{q}_v$ was mostly carried by the net mass flux through the vapor region. The latent heat of condensation was added to $\dot{q}_v$ to reproduce q_W^{cond} at the lower temperature side. The measured value of heat flux $\dot{q}_v$ was about 1/3 of $\dot{q}_w$. Then, the temperature gradient in the vapor phase is too small for the vapor heat conduction. It was revealed that the dominant carrier of energy in the vapor region was the net velocity component $<v_z>$ shown in the bottom panel of Fig. 20b. It should be noticed that when the vaporization coefficient or condensation coefficient is considered for a non-equilibrium liquid-vapor interface, the effect of this net mass flux must be removed. It seems that a considerably large vapor region should be necessary to simplify the calculation.

Matsumoto et al. [123] studied the thermal resistance between Lennard-Jones solid crystals by the direct non-equilibrium molecular dynamics. Inside a fcc crystal, one-dimensional steady heat conduction was realized using a pair of temperature controlling heat baths. Four types of atomically continuous solid-solid interfaces were investigated: (1) crystals with different masses, (2) crystals with different interaction parameters, (3) crystals with various surface interaction parameters, and (4) crystals with different size parameters. Except for

the case (4), observed temperature profiles had a discontinuity at the interface, from which the temperature jump was measured. The reduction of heat flux due to the temperature jump was larger than that predicted with a simple acoustic model.

Ohara et al. have analyzed the possible explanation of the thermal boundary resistance [124] based on their "intermolecular energy transfer" concept developed by the detailed studies of heat conduction in liquid phase water [125] and Lennard-Jones fluid [126].

II. Heat conduction of carbon nanotubes

Since most direct heat transfer problems of nanotechnology are currently related with thermophysical properties of solid materials, the heat conduction behavior of micro- and nano-devices are very important. Based on the phonon dynamics approaches [10], the direct calculation of phonon dispersion relations, phonon mean free path, and phonon scattering rates using molecular dynamics simulations are anticipated [127, 128]. As an example, the heat conduction simulation along a carbon nanotube is shown in Fig. 21 [129, 130]. The potential function employed was the simplified Brenner bond order potential [45]. The thermal conductivity of nanotubes, which was speculated to be higher than any other materials along the cylindrical axis, was measured from the simulations for nanotubes with several different chiralities and lengths. Temperature at each end of a nanotube was controlled by the phantom technique [3], and no periodic boundary condition was applied to minimize the boundary scattering of phonons. The thermal conductivity was calculated from the measured temperature gradient as in Fig. 21 and the heat flux obtained by the integration of the additional force by the phantom molecules. The preliminary result showed that the thermal conductivity was about 200 ~ 600 W/mK. The temperature jump near the heating and cooling region was explained by assuming the thermal boundary resistance due to the miss-match of the phantom technique to the structured phonon density distribution.

As the first step to connect the molecular dynamics simulation to the phonon concept approach, phonon density of states and phonon dispersion relations were extracted from the simulated trajectories. The phonon density of states was measured as the power spectra of velocity fluctuations in Eq. (58).

$$D_\alpha(\omega) = \int dt \exp(-i\omega t)\langle v_\alpha(t)v_\alpha(0)\rangle \qquad (58)$$
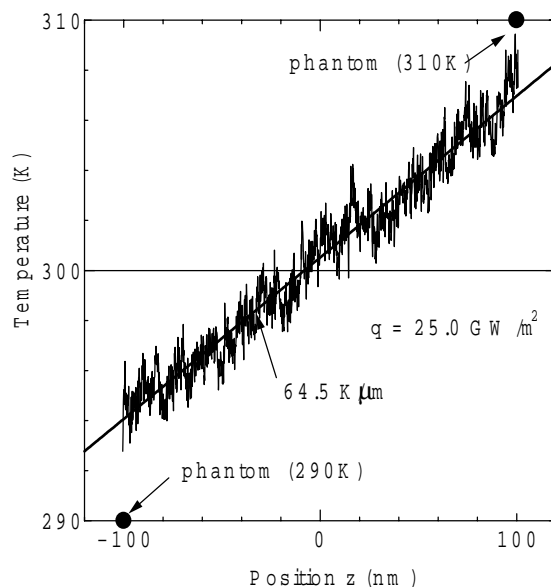
Figure 21 Molecular dynamics simulation of heat conduction along a single-walled carbon nanotube (SWNT). (a) Temperature distribution along a nanotube with (5, 5) chirality and 202 nm in length. (b) Phonon dispersion relation obtained from the time-space 2-D Fourier transform of the longitudinal displacement of each molecule.

Here, α takes r, θ, z for each velocity component in the cylindrical coordinate. The calculated density of states is shown in Fig.22 as the right hand side inserts of phonon dispersion relations. For this calculation, 8192 temporal data points saved every 5 fs were used.

The photon dispersion relations were also directly measured as the time-space 2-D Fourier transforms in Eq. (60) of the displacement vector $\mathbf{r}'(z, t)$ from the equilibrium position $r_e(z)$;

$$\mathbf{r}'(z,t) = \mathbf{r}(z,t) - \mathbf{r}_e(z) . \qquad (59)$$

$$R_\alpha'(k,\omega) = \int dt \; r_\alpha'(z,t)\exp(ikz - i\omega t) \qquad (60)$$

Here, k is the wave vector along z-axis. Position vector $r(z, t)$ of atoms in a line along z-direction separated by $a = \sqrt{3}a_{c-c}$ (a_{c-c}: bond length) are used. In the case of Figure 22, 128 data points in z direction multiplied by 8192 temporal points were used. The phonon dispersion relation obtained from eigen values and eigen vectors of dynamical matrix made with the force-constant tensor scaled from 2 D graphite [131] is shown in Figure 22(d) as the comparison. The phonon modes from radial displacement or radial velocity component in Figure 22(a) have relatively low frequency including the radial breathing mode [132]. On the other hand, the vibrational modes in the graphitic plane appear as about 1600 cm^{-1} peak in Figure 22(b) and (c). The unit cell of
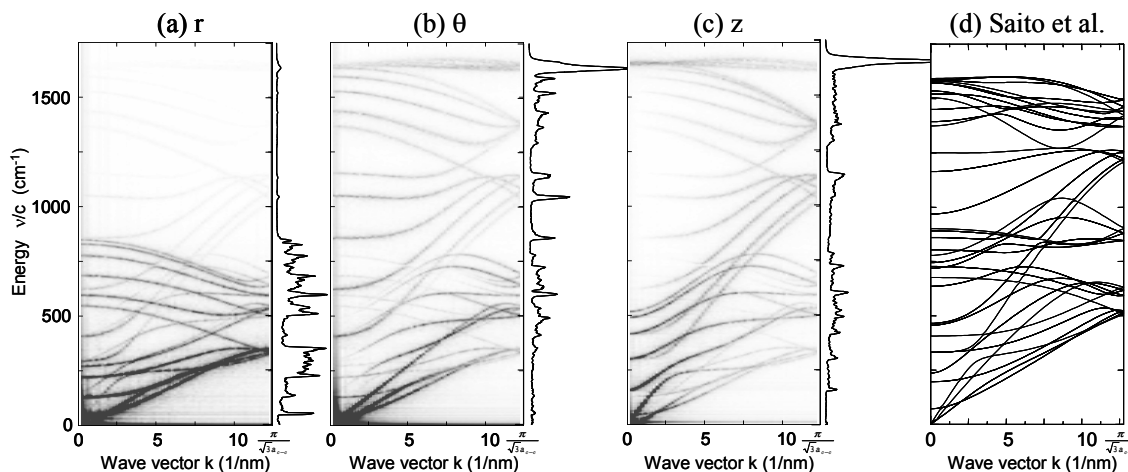
Figure 22 Phonon dispersion relation and photon density of states for 101 nm long (5, 5) SWNT. Dispersion relations from *r*, θ and *z* components of displacement are shown in (a), (b) and (c) respectively. The phonon density of states calculated as power spectra of v_r, v_θ, v_z are shown as the right hand side of dispersion relations. (d) The dispersion relations solved from the dynamical matrix using the force-constant tensor scaled from those for 2D graphite.

(5, 5) nanotube is made of 20 atoms, and there are 60 vibrational modes. Group theory for this D_{5d} symmetry structure shows that there are 12 non-degenerate and 24 doubly degenerate phonon branches [133]. Hence, there are distinguishable 36 branches of phonon dispersions in Figure 22(d). All of them were projected in Figure 22(a), (b) or (c). The group velocities of four acoustic phonons were estimated as longitudinal acoustic mode: 17 km/s (z-direction), transverse acoustic mode (degenerate): 7 km/s (r-direction), twisting acoustic

mode: 10 km/s (θ-direction), in good agreement with the dynamical matrix result in Figure 22(d).

Acknowledgements

NOMENCLATURE

A	Lennard-Jones potential parameter
a	constant in Tersoff/Brenner potential
a	lattice constant, m
a_0	equilibrium lattice constant, m
a_1-a_4	potential constants in Eq. (5), J
$\mathbf{a}_1, \mathbf{a}_2$	unit lattice vectors of honeycomb lattice
$a_{c\text{-}c}$	bond length of carbon-carbon binding, m
B	Lennard-Jones potential parameter, constant in Tersoff/Brenner potential
B	bulk modulus , Js/m^3
b_1-b_4	potential parameters in Eq. (5), 1/m
b_{ij}	bond order function in Tersoff potential
C_i	linear combination coefficients in Eq. (23)
$\mathbf{C}_h$	chiral vector
c	constant in Tersoff/Brenner potential
D	diffusivity, $m^{-2}s^{-1}$
D	half width of cutoff function, m
D_e	potential depth in Tersoff/Brenner potential eV
$D_\alpha(\omega)$	phonon density of states
$\tilde{D}_{\alpha\beta}$	rotation matrix
d	constant in Tersoff/Brenner potential
E	potential energy, J

E_k	kinetic energy, J
E_p	potential energy, J
$\tilde{E}_p$	calculated potential energy, J
E_{sub}	absolute sublimation energy at zero-temperature and pressure , J
e	charge of electron, C
$\mathbf{F}$	force vector, N
$F(\rho)$	embedding function
f	force, N
f_c	cutoff function
$g(\theta)$	a function in Tersoff/Brenner potential
$g(r)$	radial distribution functions
h	constant in Tersoff/Brenner potential
K_r, K_θ	spring constants, N/m
k	wave vector, 1/m
k_B	Boltzmann constant, 1.38066×10^{-23} J/K
m	mass, kg
N	number density, $1/m^3$
N	number of molecules
n	constant in Tersoff/Brenner potential
n, m	chiral indexes
n_s, n_d	numbers of *s*-electron and *d*-electron,

	respectively
P	pressure , Pa
$\tilde{p}$	calculated pressure, Pa
$\tilde{p}_{\alpha\beta}$	instantaneous pressure tensor, Pa
q	electric charge, C
q	heat flux, W/m^2
$\tilde{q}_a$	α (x, y, z) component of energy flux, W/m^2
$\boldsymbol{R}$	position of molecule, m
R_0	nearest neighbor distance of solid crystal, m
$R'_a(k,\omega)$	2-D Fourier transform
$R_i(r)$	atomic electron density function
R_e	equilibrium intermolecular distance, m
R_T	thermal boundary resistance, m^{2}K/W
r	intermolecular distance, m
$\boldsymbol{r}$	position vector, m
S	shape factor in Morse potential
S	entropy, J/K
T	temperature, K
T_C	control temperature, K
T_c	critical temperature, K
T_{JUMP}	temperature jump, K
T_t	triplet temperature, K
t	time, s
t_P	time constant, s
U	internal energy, J
V	volume, m^3
V_0-V_3, V_n	Fourier coefficients in Eq. (9), J
$V_A(r)$	an attractive potential function in Tersoff/Brenner potential
$V_R(r)$	a repulsive potential function in Tersoff/Brenner potential
$\boldsymbol{v}$	velocity vector, m/s
Z_0	number of electrons
$Z(R)$	effective charge function
z	coordinate perpendicular to the interface, m

Greek Symbols

α	isotropic polarizability, Cm^{2}V^{-1} (in SI)
α	constant in Eq. (26)
β	constant in Morse type potential, 1/m
β	constant in Eq. (26)
β_T	isothermal compressibility
χ	scaling factor in Eq. (33)
Δr	parameter of extension of interface
Δt	time step of the finite difference integration s
δ	constant in Tersoff/Brenner potential
ε	energy parameter of Lennard-Jones potential, J
ε_0	permittivity (dielectric constant) in vacuum = 8.8542×10^{-12} F/m = 8.8542×10^{-12} C^2/(Nm^2)

ε_i	instantaneous energy of molecule *i,* J
Φ	potential , J
ϕ	pair potential, J
ϕ	dihedral angle
γ	surface tension, surface energy, N/m^2
λ	thermal conductivity, W/(mK)
μ	shear viscosity, Pa s
ν	potential constant in Eq. (26)
θ	angle, contact angle
θ_t	tetrahedral angle
θ_∞	asymptotic contact angle for macroscopic system
ρ	number density, 1/m^3
ρ	electron density
σ	length parameter of Lennard-Jones potential, m
σ_F	standard deviation of exiting force, N
τ	time scale of non-dimensional Lennard-Jones system: $\tau = \sigma(m/\varepsilon)^{1/2}$, s
ω	angular frequency, rad/s
Ω	phase space volume, equilibrium volume per atom
ζ	friction coefficient, 1/s
ζ	effective atomic charge divided by effective quantum number

Subscripts

AR	argon
C	cutoff, control, center of fitting circle
d	*d* electron
G	gas
H	hydrogen
H$_2$O	water
INT	interaction of solid and liquid
i, j, k	index of molecule
L	liquid
LR	long-range correction
LG	liquid-gas
M	position of negative point charge
N	normal direction
O	oxygen
Pt	platinum
S	solid
s	*s* electron
SG	solid-gas
SL	solid-liquid
SURF	surface, surface integrated
T	tangential direction
V	vapor
W	solid wall

REFERENCES

[1]   M. P. Allen and D. J. Tildesley, *Computer Simulation of Liquids*, Oxford University Press, New York, 1987.

[2]   J. M. Haile, *Molecular Dynamics Simulation*, Wiley, New York, 1992.

[3]   S. Maruyama, "Molecular Dynamics Method for Microscale Heat Transfer," *Advances in Numerical Heat Transfer*, vol. 2, ed. W. J. Minkowycz and E. M. Sparrow, Taylor & Francis, pp. 189-226, 2000.

[4]   T. Ohara, "Molecular Dynamics Study in Microscale Thermophysical Engineering: Current Activities and Future in Japan," *Micro. Thermophys. Eng.*, Vol. 4, No. 4, pp. 213-221, 2000.

[5]   D. Poulikakos, S. Arcidiacono and S. Maruyama, "Molecular Dynamics Simulations in Nanoscale Heat Transfer: A Review," *Micro. Thermophys. Eng.*, submitted.

[6]   A. Majumdar, "Nanoengineering: Promises and Challenges," *Micro. Thermophys. Eng.*, Vol. 4, No. 2, pp. 77-82, 2000.

[7]   J. O. Hirschfelder, C. F. Curtiss and R. B. Bird, *Molecular Theory of Gases and Liquids*, John Wiley & Sons, New York, 1954.

[8]   G. A. Bird, *Molecular Gas Dynamics and the Direct Simulation of Gas Flow*, Oxford University Press, New York, 1994.

[9]   C. Kittel, *Introduction to Solid State Physics*, 7th ed., John Wiley & Sons, New York, 1996.

[10] G. Chen, Thermal Conductivity and Ballistic-Phonon Transport in the Cross-Plane Direction of Superlattices, *Phys. Rev. B*, vol. 57, no. 23, pp. 14958-14973, 1998.

[11] J. J. Nicolas , K. E. Gubbins, W. B. Streett and D. J. Tildesley, Equation of State for the Lennard-Jones Fluid, *Molecular Physics*, vol. 37-5, pp. 1429-1454, 1979.

[12] F. H. Lee, Analytic Representation of Thermodynamics Data for the Lennard-Jones Fluid, *J. Chem. Phys.*, vol. 73, no. 10, pp. 5401-5403, 1980.

[13] J. P. Hansen and L. Verlet, Phase Transitions of the Lennard-Jones System, *Phys. Rev.*, vol. 184, pp. 151-161, 1969.

[14] S. D. Stoddard and J. Ford, Numerical Experiments on the Stochastic Behavior of a Lennard-Jones Gas System, *Phys. Rev. A*, vol. 8, pp. 1504-1512, 1973.

[15] M. J. P. Nijmeijer, A. F. Bakker, C. Bruin, and J. H. Sikkenk, A Molecular Dynamics Simulation of the Lennard-Jones Liquid-Vapor Interface, *J. Chem. Phys.*, vol. 89, no. 6, pp. 3789-3792, 1988.

[16] F. H. Stillinger and A. Rahman, Improved Simulation of Liquid Water by Molecular Dynamics, *J. Chem. Phys.*, vol. 60, no. 4, pp. 1545-1557, 1974.

[17] A. Ben-Naim and F. H. Stillinger, Aspects of the Statistical-Mechanical Theory of Water, in Structure and Transport Processes in *Water and Aqueous Solutions* (ed. R. A. Horne), Wiley-Interscience, New York, 1972.

[18] H. J. C. Berendsen, J. P. M. Postma, W. F. van Gunsteren, J. Hermans, in *Intermolecular Forces* (ed. B. Pullmann), Reidel, Dordrecht, pp. 331-, 1981.

[19] H. J. C. Berendsen, J. R. Grigera, and T. P. Straatsma, The Missing Term in Effective Pair Potentials, *J. Phys. Chem.*, vol. 91, no. 24, pp.6269-6271, 1987.

[20] W. L. Jorgensen, J. Chandrasekhar, J. D. Madura, R. W. Impey and M. L. Klein, Comparison of Simple Potential Functions for Simulating Liquid Water, *J. Chem. Phys.*, vol. 79, no. 2, pp. 926-935, 1983.

[21] W. L. Jorgensen, Optimized Intermolecular Potential Functions for Liquid Alcohols, *J. Phys. Chem.*, vol. 90, pp. 1276-1284, 1986.

[22] O. Matsuoka, E. Clementi and M. Yoshimine, CI Study of the Water Dimer Potential Surface, *J. Chem. Phys.*, vol. 64, no. 4, pp. 1351-1361, 1976.

[23] V. Carravetta and E. Clementi, Water-Water Interaction Potential: An Approximation of the Electron Correlation Contribution by a Function of the SCF Density Matrix, *J. Chem. Phys.*, vol. 81, no. 6, pp. 2646-2651, 1984.

[24] J. Alejandre, D. J. Tildesley, and G. A. Chapela, Molecular Dynamics Simulation of the Orthobaric Densities and Surface Tension of Water, *J. Chem. Phys.*, vol. 102, no. 11, pp. 4574-4583, 1995.

[25] L. X. Dang, and T-M. Chang, Molecular Dynamics Study of Water Clusters, Liquid, and Liquid-Vapor Interface of Water with Many-Body Potentials, *J. Chem. Phys.*, vol. 106, no. 19, pp. 8149-8159, 1997.

[26] U. Niesar, G. Corongiu, E. Clementi, G. R. Kneller and D. K. Bhattacharya, Molecular Dynamics Simulations of Liquid Water Using the NCC ab initio Potential, *J. Phys. Chem.*, vol. 94, no. 20, pp. 7949-7956, 1990.

[27] D. N. Bernardo, Y. Ding, K. K-Jespersen and R. M. Levy, An Anisotropic Polarizable Water Model: Incorporation of All-Atom Polarizabilities into Molecular Mechanics Force Fields, *J. Phys. Chem.*, vol. 98, pp. 4180-4187, 1994.

[28] L. X. Dang and B. M. Pettitt, Simple Intramolecular Model Potentials for Water, *J. Phys. Chem.*, vol. 91, no. 12, pp. 3349-3354, 1987.

[29] J. Anderson, J. J. Ullo and S. Yip, Molecular Dynamics Simulation of Dielectric Properties of Water, *J. Chem. Phys.*, vol. 83, no. 3, pp. 1726-1732, 1987.

[30] W. L. Jorgensen, J. D. Madura and C. J. Swenson, Optimized Intermolecular Potential Functions for Liquid Hydrocarbons, *J. Am. Chem. Soc.*, 106, 6638 (1984).

[31] J. P. Hansen and I. R. McDonald, Theory of Simple Liquids, 2nd ed. (Academic, London, 1986).

[32] S. J. Weiner, P. A. Kollman, D. A. Case, U. C. Singh, C. Ghio, G. Alagona, S. Profeta, Jr. and P. Weiner, A new force field for molecular mechanical simulation of nucleic acids and proteins, *J. Am. Chem. Soc.*, vol. 106, pp. 765-784, 1984.

[33] S. J. Weiner, P. A. Kollman, D. T. Nguyen and D. A. Case, An all-atom force field for simulations of proteins and nucleic acids, *J. Computat. Chem.*, vol. 7, pp. 230-252, 1986.

[34] W. D. Cornell, P. Cieplak, C. I. Bayly, I. R. Gould, K. M. Merz, Jr., D. M. Ferguson, D. C. Spellmeyer, T. Fox, J. W. Caldwell and P. A. Kollman, A Second Generation Force Field for the Simulation of Proteins, Nucleic Acids, and Organic Molecules, *J. Am. Chem. Soc.*, vol. 117, pp. 5179-5197, 1995.

[35] R. W. Dixon and P. A. Kollman, Advancing Beyond the Atom- Centered Model in Additive and Nonadditive Molecular Mechanics, *J. Computat. Chem.*, vol. 18, pp. 1632-1646, 1997.

[36] J. Wang, P. Cieplak and P.A. Kollman, How well does a restrained electrostatic potential (RESP) model perform in calcluating conformational energies of organic and biological molecules, *J. Computat. Chem.*, vol. 21, pp. 1049-1074, 2000.

[37] P. Cieplak, J. Caldwell and P. Kollman, Molecular Mechan- ical Models for Organic and Biological Systems Going Beyond the Atom Centered Two Body Additive Approximation: Aqueous Solution Free Energies of Methanol and N- Methyl Acetamide, Nucleic Acid Base, and Amide Hydrogen Bonding and Chloroform/Water Partition Coefficients of the Nucleic Acid Bases, *J. Computat. Chem.*, vol. 22, pp. 1048-1057, 2001.

[38] http://www.amber.ucsf.edu/amber/amber.html

[39] D.A. Pearlman, D.A. Case, J.W. Caldwell, W.S. Ross, T.E. Cheatham, III, S. DeBolt, D. Ferguson, G. Seibel and P. Kollman, AMBER, a package of computer programs for applying molecular mechanics, normal mode analysis, molecular dynamics and free energy calculations to simulate the structural and energetic properties of molecules, *Comp. Phys. Commun.*, vol. 91, pp. 1-41, 1995.

[40] D.A. Case, D.A. Pearlman, J.W. Caldwell, T.E. Cheatham III, J. Wang, W.S. Ross, C.L. Simmerling, T.A. Darden, K.M. Merz, R.V. Stanton, A.L. Cheng, J.J. Vincent, M. Crowley, V. Tsui, H. Gohlke, R.J. Radmer, Y. Duan, J. Pitera, I. Massova, G.L. Seibel, U.C. Singh, P.K. Weiner and P.A. Kollman (2002), AMBER 7, University of California, San Francisco.

[41] F. H. Stillinger and T. A. Weber, Computer Simulation of Local Order in Condensed Phase of Silicon, *Phys. Rev. B*, vol. 31, no. 8, pp. 5262-5271, 1985.

[42] J. Tersoff, New Empirical Approach for the Structure and Energy of Covalent Systems, *Phys. Rev. B*, vol. 37, no. 12, pp. 6991-7000, 1988.

[43] J. Tersoff, Empirical Interatomic Potential for Silicon with Improved Elastic Properties, *Phys. Rev. B*, vol. 38, no. 14, pp. 9902-9905, 1988.

[44] J. Tersoff, Modeling Solid-State Chemistry: Interatomic Potentials for Multicomponent Systems, *Phys. Rev. B*, vol. 39, no. 8, pp. 5566-5568, 1989.

[45] D. W. Brenner, Empirical Potential for Hydrocarbons for Use in Simulating the Chemical Vapor Deposition of Diamond Films, *Phys. Rev. B*, vol. 42, pp.9458-9471, 1990.

[46] Y. Yamaguchi and S. Maruyama, A Molecular Dynamics Simulation of the Fullerene Formation Process, *Chem. Phys. Lett.*, vol. 286-3,4, pp. 336-342, 1998.

[47] S. Maruyama and Y. Yamaguchi, A Molecular Dynamics Demonstration of Annealing to a Perfect C_{60} Structure, *Chem. Phys. Lett.*, vol. 286-3,4, pp. 343-349, 1998.

[48] http://www.mse.ncsu.edu/CompMatSci/

[49] D. W. Brenner, O. A. Shenderova, J. A. Harrison, S. J. Stuart, B. Ni and S. B. Sinnott, A Second-Generation Reactive Empirical Bond Order (REBO) Potential Energy Expression for Hydrocarbons, *J. Phys.: Condens. Matter*, vol. 14, pp. 783-802, 2002.

[50] L. A. Girifalco and V. G. Weizer, Application of the Morse Potential Function to Cubic Metals, *Phys. Rev.*, vol. 114, pp. 687-690, 1959.

[51] R. A. Johnson, Empirical Potentials and Their Use in the Calculation of Energies of Point Defects in Metals, *J. Phys. F: Metal Phys.*, vol. 3, pp. 295-321, 1973.

[52] M. S. Daw and M. I. Baskes, Semiempirical, Quantum Mechanical Calculation of Hydrogen Embrittlement in Metals, *Phys. Rev. Lett.*, vol. 50, pp. 1285-1288, 1983.

[53] M. S. Daw and M. I. Baskes, Embedded-Atom Method: Derivation and Application to Impurities, Surfaces, and Other Defects in Metals, *Phys. Rev. B*, vol. 29, pp. 6443-6453, 1984.

[54] S. M. Foiles, M. I. Baskes, and M. S. Daw, Embedded-Atom-Method Functions for the fcc Metals Cu, Ag, Au, Ni, Pd, Pt, and Their Alloys, *Phys. Rev. B*, vol. 33, pp. 7983-7991, 1986.

[55] M. I. Baskes, Application of the Embedded-Atom Method to Covalent Materials: A Semiempirical Potential for Silicon, *Phys. Rev. Lett.*, vol. 59, pp. 2666-2669, 1987.

[56] M. I. Baskes, J. S. Nelson, and A. F. Wright, Semiempirical Modified Embedded-Atom Potentials for Silicon and Germanium, *Phys. Rev. B*, vol. 40, pp. 6085-6100, 1989.

[57] M. I. Baskes, Modified Embedded-Atom Potentials for Cubic Materials and Impurities, *Phys. Rev. B*, vol. 46, pp. 2727-2742, 1992.

[58] M. I. Baskes and R. A. Johnson, Modified Embedded Atom Potentials for HCP Metals, *Modelling Simul. Mater. Sci. Eng.*, vol. 2, pp. 147-163, 1994.

[59] M. I. Baskes, J. E. Angelo and C. L. Bisson, Atomistic Calculations of Composite Interfaces, *Modelling Simul. Mater. Sci. Eng.*, vol. 2, pp. 505-518, 1994.

[60] E. Clementi and C. Roetti, Roothaan-Hartree-Fock Atomic Wavefunctions - Basis Functions and Their Coefficients for Ground and Certain Excited States of Neutral and Ionized Atoms, Z < 54, *Atomic Data and Nuclear Data Tables* (Academic, New York), vol. 14, nos. 3, 4, pp. 177-478, 1974.

[61] J. H. Rose, J. R. Smith, F. Guinea, J. Ferrante, Universal features of the equation of state of metals, *Phys. Rev. B*, vol. 29, pp. 2963-2969, 1984.

[62] D. H. Tsai, The Virial Theorem and Stress Calculation in Molecular Dynamics, *J. Chem. Phys.*, vol. 70, no. 3, pp. 1375-1382, 1979.

[63] B. Hafskjold and T. Ikeshoji, Microscopic Pressure Tensor for Hard-Sphere Fluids, Phys. Rev. E, vol. 66, pp. 011203/1-011203/4, 2002.

[64] H. C. Anderson, Molecular Dynamics Simulations at Constant Pressure and/or Temperature, *J. Chem. Phys.*, vol. 72, no. 4, pp. 2384-2393, 1980.

[65] S. Nosé, A Unified Formulation of the Constant Temperature Molecular Dynamics Methods, *J. Chem. Phys.*, vol. 81, no. 1, pp. 511-519, 1984.

[66] W. G. Hoover, Canonical Dynamics: Equilibrium Phase-Space Distributions, *Phys. Rev. A*, vol. 31, no. 3, pp. 1695-1697, 1985.

[67] M. Parrinello and A. Rahman, Crystal Structure and Pair Potentials: a Molecular Dynamics Study, *Phys. Rev. Lett.*, vol. 45, pp. 1196-1199, 1980.

[68] M. Parrinello and A. Rahman, Polymorphic Transitions in Single Crystal: a New Molecular Dynamics Method, *J. Appl. Phys.*, vol. 52, pp. 7182-7190, 1981.

[69] H. J. C. Berendsen, J. P. M. Postma, W. F. van Gunsteren, A. DiNola, and J. R. Haak, Molecular dynamics with coupling to an external bath, *J. Chem. Phys.*, vol. 81, no. 8, pp. 3684-3690, 1984.

[70] M. J. P. Nijmeijer, A. F. Bakker, C. Bruin and J. H. Sikkenk, A Molecular Dynamics Simulation of the Lennard-Jones Liquid-Vapor Interface, *J. Chem. Phys.*, vol. 89, no. 6, pp. 3789-3792, 1988

[71] J. Alejandre, D. J. Tildesley and G. A.Chapela, Molecular Dynamics Simulation of the Orthobaric Densities and Surface Tension of Water, *J. Chem. Phys.*, vol. 102, no. 11, pp. 4574-4583, 1995.

[72] S. M. Thompson, K. E. Gubbins, J. P. R. B. Walton, R. A. R. Chantry, and J. S. Rowlinson, A Molecular Dynamics Study of Liquid Drops, *J. Chem. Phys.*, vol. 81, no. 1, pp. 530-542,1984.

[73] K. Yasuoka, M. Matsumoto and Y. Kataoka, Evaporation and Condensation at a Liquid Surface. I. Argon, *J. Chem. Phys.,* vol. 101, no. 9, pp. 7904-7911, 1994.

[74] M. Matsumoto, K. Yasuoka and Y. Kataoka, Evaporation and Condensation at a Liquid Surface. II. Methanol, *J. Chem. Phys.*, vol. 101, no. 9, pp. 7911-7917, 1994.

[75] T. Tsuruta, H. Tanaka, K. Tamashima and T. Masuoka, Condensation Coefficient and Interphase Mass Transfer, *International Symposium on Molecular and Microscale Heat Transfer in Materials Processing and Other Applications* (ed. I. Tanasawa and S. Nishio), Begell House, New York, pp. International Center Heat Mass Transfer Symposium, Yokohama, pp. 229-240, 1997.

[76] H. Daiguji, "Molecular dynamics study of n-alcohols adsorbed on an aqueous electrolyte solution," *J. Chem. Phys.*, vol. 115, no. 4, pp. 1538-1549, 2001.

[77] V. E. B. Dussan, On the Spreading of Liquids on Solid Surfaces: Static and Dynamic Contact Lines, *Ann. Rev. Fluid Mech.*, vol. 11, pp. 371-400, 1979.

[78] J. Koplik and J. R. Banavar, Continuum Deductions from Molecular Hydrodynamics, *Ann. Rev. Fluid Mech.*, vol. 27, pp. 257-292, 1995.

[79] S. Matsumoto, S. Maruyama, and H. Saruwatari, A Molecular Dynamics Simulation of a Liquid Droplet on a Solid Surface, Proceedings of the ASME-JSME Thermal Engineering Joint Conference, Maui, U.S.A., March 19-24, 1995, Vol. 2, pp. 557-562, 1995.

[80] S. Maruyama, T. Kurashige, S. Matsumoto, Y. Yamaguchi and T. Kimura, Liquid Droplet in Contact with a Solid Surface, Micro. Thermophys. Eng., vol. 2, no.1, pp. 49-62, 1998.

[81] S. Maruyama, T. Kimura and M.-C. Lu, Molecular Scale Aspects of Liquid Contact on a Solid Surface, *Therm. Sci. Eng.*, vol. 10, no.6, 2002, in press.

[82] S. Maruyama and T. Kimura, A Molecular Dynamics Simulation of a Bubble Nucleation on Solid Surface, *Int. J.*

Heat & Technology, vol. 8, no. 1, pp. 69-74, 2000.

[83] T. Kimura and S. Maruyama, Molecular dynamics simulation of water droplet in contact with platinum surface, *Proc. 12th Int. Heat Transfer Conf.*, Grenoble, pp. 537-542, 2002.

[84] S.-B.Zhu and M. R. Philpott, Interaction of Water with Metal Surfaces, *J. Chem. Phys.*, vol. 100, no. 9, pp. 6961-6968, 1994.

[85] S. Iijima, Helical microtubules of graphitic carbon, *Nature*, vol. 354, pp. 56-58, 1991.

[86] S. Iijima and T. Ichihashi, Single-Shell Carbon Nanotubes of 1-nm Diameter, *Nature*, vol. 363, pp. 603-605, 1993.

[87] M. S. Dresselhaus and G. Dresselhaus, *Science of Fullerenes and Carbon Nanotubes*, Academic Press, New York, 1996.

[88] R. Saito, G. Dresselhaus and M. S. Dresselhaus, *Physical Properties of Carbon Nanotubes*, Imperial College Press, London, 1998.

[89] A. Thess, R. Lee, P. Nikolaev, H. Dai, P. Petit, J. Robert, C. Xu, Y. H. Lee, S. G. Kim, A. G. Rinzler, D. T. Colbert, G. E. Scuseria, D. Tománek, J. E. Fischer and R. E. Smalley, Crystalline Ropes of Metallic Carbon Nanotubes, *Science*, vol. 273, pp. 483-487, 1996.

[90] C. Journet, W. K. Maser, P. Bernier, A. Loiseau, M. L. de la Chapelle, S. Lefrant, P. Deniard, R. Lee and J. E. Fisher, Large-Scale Production of Single-Walled Carbon Nanotubes by the Electric-Arc Technique, *Nature*, vol. 388, pp. 756-758, 1997.

[91] M. J. Bronikowski, P. A. Willis, D. T. Colbert, K. A. Smith and R. E. Smalley, Gas-phase Production of Carbon Single-Walled Nanotubes from Carbon Monoxide via the HiPco Process: A Parametric Study, *J. Vac. Sc. Technol. A*, vol. 19, pp. 1800-1805, 2001.

[92] S. Maruyama, R. Kojima, Y. Miyauchi, S. Chiashi and M. Kohno, Low-Temperature Synthesis of High-Purity Single-Walled Carbon Nanotubes from Alcohol, Chem. Phys. Lett., 360-3-4, 229-234, 2002.

[93] A. C. Dillon, K. M. Jones, T. A. Bekkedahl, C. H. Kiang, D. S. Bethune and M. J. Heben, Storage of Hydrogen in Single-Walled Carbon Nanotubes, *Nature*, vol. 386-27, pp. 377-379, 1997.

[94] Y. Ye, C. C. Ahn, C. Witham, B. Fultz, J. Liu, A. G. Rinzler, D. Colbert, K. A. Smith, and R. E. Smalley, Hydrogen Adsorption and Cohesive Energy of Single-Walled Carbon Nanotubes,*Appl. Phys. Lett.*, vol. 74-16, pp. 2307-2309, 1999.

[95] C. Liu, Y. Y. Fan, M. Liu, H. T. Cong, H. M. Cheng and M. S. Dresselhaus, Hydrogen Storage in Single-Walled Carbon Nanotubes at Room Temperature, *Science*, vol. 286-5, pp. 1127-1129, 1999.

[96] G. G. Tibbetts , G. P. Meisner, C. H. Olk, Hydrogen storage capacity of carbon nanotubes, filaments, and vapor-grown fibers, *Carbon* vol. 39, pp. 2291-2301, 2001.

[97] Q. Wang and J. K. Johnson, Molecular simulation of hydrogen adsorption in single-walled carbon nanotubes and idealized carbon slit pores, *J. Chem. Phys.*, vol. 110, no. 1, pp. 577-586, 1999.

[98] K.A. Williams and P.C. Eklund, Monte Carlo simulations of H2 physisorption in finite-diameter carbon nanotube ropes, *Chem. Phys. Lett.*, vol. 320, pp. 352-358, 2000.

[99] S. Maruyama and T. Kimura, Molecular Dynamics Simulation of Hydrogen Storage in Single-Walled Carbon Nanotubes, Proc. ASME Heat Transfer Division 2000, Orlando, vol. 2, pp. 405-409, 2000.

[100] Y. Gototsi, J.A. Libera, A.G. Güvenç-Yazicioglu and C.M. Megaridis, In Situ Multiphase fluid Experiments in Hydrothermal Carbon Nanotubes, *Appl. Phys. Lett.*, vol.79, no 7, pp. 1021-1023, 2001

[101] C. M. Megaridis, A. G. Güvenç-Yazicioglu, J. A. Libera, and Y. Gototsi, Attoliter Fluid experiments in Individual Closed-End Carbon Nanotubes: Liquid Film and Fluid Interface Dynamics, Phys. Fluids, vol.14, no 2, L5-L8, 2002.

[102] E. Dujardin, T. W. Ebbesen, H. Hiura, K. Tanigaki, Capillary and Wetting of Carbon Nanotubes, *Science*, vol. 265, pp. 1850-1852, 1994.

[103] J. H. Walther, R. Jaffe, T. Halcioglou and P. Koumoutsakos, Carbon Nanotubes in water; Structural Characteristics and Energetics, *J. Phys. Chem. B*, vol.105, pp. 9980-9987, 2001.

[104] T. Werder, J. H. Walther, R .L. Jaffe, T. Halicioglu, F. Noca and P. Koumoutsakos, "Molecular Dynamics Simulation of Contact Angles of Water Droplets in Carbon Nanotubes," *NanoLetters*, vol. 1, no 12, pp. 697-702, 2001.

[105] K.Yasuoka and M. Matsumoto, Molecular Dynamics of Homogeneous Nucleation in the Vapor Phase. I. Lennard-Jones Fluid, *J. Chem. Phys.*, vol. 109, no. 19, pp. 8451-8462, 1998.

[106] K. Yasuoka and M. Matsumoto, Molecular Dynamics of Homogeneous Nucleation in the Vapor Phase. II. Water, *J. Chem. Phys.*, vol. 109, no. 19, pp. 8463-8470, 1998.

[107] T. Ikeshoji, B. Hafskjold, Y. Hashi, and Y. Kawazoe, Molecular Dynamics Simulation for the Formation of Magic-Number Clusters with the Lennard-Jones Potential, *Phys. Rev. Lett.*, vol. 76, no. 11, pp. 1792-1795, 1996.

[108] T. Kimura and S. Maruyama, A Molecular Dynamics Simulation of Heterogeneous Nucleation of a Liquid

Droplet on Solid Surface, *Micro. Thermophys. Eng.*, vol. 6, no. 1, pp. 3-13, 2002.

[109] T. Kinjo and M. Matsumoto, "Cavitation Processes and Negative Pressure," *Fluid Phase Equilibria*, vol. 144, pp. 343-350, 1998.

[110] S. Maruyama and T. Inoue, MD Simulation of Crystallization Process of Silicon, *Proc. 38th Japan Heat Transfer Conf.*, 38-343, 2001.

[111] G. H. Gilmer, H. Huang and C. Roland, Thin film deposition: fundamentals and modeling, *Comp. Mat. Sci.*, vol. 12, pp. 354-380, 1998.

[112] Y. Yamaguchi and S. Maruyama, A Molecular Dynamics Study on the Formation of Metallofullerene, *Euro. Phys. J. D*, vol. 9, no. 1-4, pp. 385-388, 1999.

[113] Y. Shibuta and S. Maruyama, Molecular Dynamics Simulation of Generation Process of SWNTs, *Physica B*, vol. 323, no. 1-4, pp. 187-189, 2002.

[114] J.-F. Colomer, C. Stephan, S. Lefrant, G. Van Tendeloo, I. Willems, Z. Konya, A. Fonseca, Ch. Laurent and J. B.Nagy, Large-scale synthesis of single-wall carbon nanotubes by catalytic chemical vapor deposition (CCVD) method, *Chem. Phys. Lett.*, vol. 317, pp. 83-89, 2000.

[115] Y. Shibuta and S. Maruyama, A Molecular Dynamics Simulation of Formation Process of SWNTs in CCVD Method, 6th ASME/JSME Thermal Engng. Conf., Hawaii, 2003, in press.

[116] D. J. Evans, Homogeneous NEMD Algorithm for Thermal Conductivity: Application of Non-Canonical Linear Response Theory, *Phys. Lett.*, 91A, 457-460, 1982.

[117] D. J. Evans and G. P. Morriss, Statistical Mechanics of Non Equilibrium Liquids, Academic Press, London 1990.

[118] R. Vogelsang, C. Hoheisel and G. Ciccotti, Thermal Conductivity of the Lennard-Jones Liquid by Molecular Dynamics Calculations, *J. Chem. Phys.,* vol. 86, pp. 6371-, 1987.

[119] P. K. Schelling, S. R. Phillpot and P. Keblinski, Comparison of Atomic-Level Simulation Methods for Computing Thermal Conductivity, *Phys. Rev. B*, vol. 65, pp. 144306/1-144306/12, 2002.

[120] B. Hafskjold and T. Ikeshoji, On the Molecular Dynamics Mechanism of Thermal Diffusion in Liquids, *Molecular Physics*, vol. 80, no. 6, pp. 1389-1412, 1993.

[121] T. Ikeshoji and B. Hafskjold, Non-Equilibrium Molecular Dynamics Calculations of Heat Conduction in Liquid and through Liquid-Gas Interface, *Molecular Physics*, vol. 81, no. 2, pp. 251-261, 1994.

[122] S. Maruyama and T. Kimura, A Study on Thermal Resistance over a Solid-Liquid Interface by the Molecular Dynamics Method, *Thermal Sci. Eng.*, vol. 7, no. 1, pp. 63-68, 1999.

[123] M. Matsumoto, H. Wakabayashi and T. Makino, Thermal Resistance of Crystal Interface: Molecular Dynamics Simulation, *Trans. JSME, Ser. B*, vol. 68, no. 671, pp. 1919-1925, 2002.

[124] T. Ohara and D. Suzuki, Intermolecular Energy Transfer at a Solid-Liquid Interface, *Micro. Thermophys. Eng.*, vol. 4, No. 3, pp. 189-196, 2000.

[125] T. Ohara, Intermolecular Energy Transfer in Liquid Water and Its Contribution to Heat Conduction: An Molecular Dynamics Study, *J. Chem. Phys.*, vol. 111, pp. 6492-6500, 1999.

[126] T. Ohara, Contribution of Intermolecular Energy Transfer to Heat Conduction in a Simple Liquid, *J. Chem. Phys.*, vol. 111, pp. 9667-9672, 1999.

[127] C. L. Tien, J. R. Lukes and F.-C.Chou, Molecular Dynamics Simulation of Thermal Transport in Solids, Micro. Thermophys. Eng., vol. 2, pp. 133-137, 1998.

[128] M. Matsumoto, M. Komiyama, T. Makino. and H. Wakabayashi, MD Simulation and Phonon Analysis for Heat Conduction in Solids, *Proc. 37th Japan Heat Transfer Conf.*, vol. 3, pp. 975-976, 2000.

[129] S. Maruyama, A Molecular Dynamics Simulation of Heat Conduction of Finite Length SWNTs, *Physica B*, vol. 323, no. 1-4, pp. 193-195, 2002.

[130] S. Maruyama, A Molecular Dynamics Simulation of Heat Conduction of a Finite Length Single-Walled Carbon Nanotube, *Micro. Thermophys. Eng.*, 2002 in press.

[131] R. Saito, T. Takeya, T. Kimura, G. Dresselhaus, and M. S. Dresselhaus, Raman Intensity of Single-Walled Carbon Nanotubes, *Phys. Rev. B*, vol. 57, pp. 4145-4153, 1998.

[132] A. M. Rao, E. Richter, S. Bandow, B. Chase, P. C. Eklund, K. A. Williams, S. Fang, K. R. Subbaswamy, M. Menon, A. Thess, R. E. Smalley, G. Dresselhaus and M. S. Dresselhaus, Diameter-Selective Raman Scattering from Vibrational Modes in Carbon Nanotubes, *Science*, vol. 275, pp. 187-191, 1997.

[133] M. S. Dresselhaus and P. C. Eklund, Phonons in Carbon Nanotubes, *Adv. Phys.*, vol. 49, pp. 705-814, 2000.